Research Square

Preprints are preliminary reports that have not undergone peer review.
They should not be considered conclusive, used to inform clinical practice,
or referenced by the media as validated information.

Albumin-binding nanobody cancer vaccines coordinate lymphatic T cell priming and inflammatory remodeling of the tumor microenvironment

John Wilson

john.t.wilson@vanderbilt.edu

Vanderbilt University https://orcid.org/0000-0002-9144-2634

Hayden Pagendarm

Vanderbilt University https://orcid.org/0000-0001-7611-6120

Neil Chada

Vanderbilt University https://orcid.org/0000-0003-4566-3564

Taylor Patino

Vanderbilt University

Alexander Kwiatkowski

Vanderbilt University https://orcid.org/0000-0001-5435-3555

Mia Woodruff

Vanderbilt University

Jacob Schulman

Vanderbilt University

Katherine Young

Vanderbilt University

Christopher Lofts

Vanderbilt University

Emmanuela Adjei-Sowah

Vanderbilt University

Anastasia Varanko

Vanderbilt University

Jonah Finkelstein

Vanderbilt University

Alexandra Lee

Vanderbilt University

Hailey Frank

Vanderbilt University

Jody May
https://orcid.org/0000-0003-4871-5024
Landon Clark
Vanderbilt University
Rachel Bonami
Vanderbilt Health https://orcid.org/0000-0001-7575-6943
John McLean
Department of Chemistry and Center for Innovative Technology, Vanderbilt University
https://orcid.org/0000-0001-8918-6419
Blaise Kimmel
The Ohio State University https://orcid.org/0000-0002-9582-9887
Karan Arora
Vanderbilt University https://orcid.org/0000-0003-1472-1637

Article

Keywords:

Posted Date: November 9th, 2026

DOI: https://doi.org/10.21203/rs.3.rs-11076444/v1

License: This work is licensed under a Creative Commons Attribution 4.0 International License.
Read Full License

Additional Declarations: Yes there is potential Competing Interest. J.T.W., H.M.P., B.R.K., and K.A. have patent PCT/US2024/051131 pending to Vanderbilt University. J.T.W. has received consulting fees from ADC Therapeutics and has received sponsored research support from Incyte Corporation.

TITLE

Albumin-binding nanobody cancer vaccines coordinate lymphatic T cell priming and inflammatory remodeling of the tumor microenvironment

AUTHORS

Hayden M. Pagendarm[1,2], Neil C. Chada[1], Taylor M. Patino[2], Alexander J. Kwiatkowski[2], Mia E. Woodruff[1], Jacob A. Schulman[1], Katherine A. Young[1], Christopher Lofts[3], Emmanuela Adjei-Sowah[2], Anastasia K. Varanko[2], Jonah E. Finkelstein[2], Alexandra Lee[2], Hailey J. Frank[2], Jody C. May[3-6], Landon M. Clark[7], Rachel H. Bonami[7-10], John A. McLean[3-6], Blaise R. Kimmel[2,11], Karan Arora[2], John T. Wilson[1,2,5-7,9,10]*

AFFILIATIONS

[1]Department of Biomedical Engineering, Vanderbilt University, Nashville, TN 37235, USA

[2]Department of Chemical and Biomolecular Engineering, Vanderbilt University, Nashville, TN 37235, USA

[3]Department of Chemistry, Vanderbilt University, Nashville, TN 37235, USA

[4]Vanderbilt Center for Innovative Technology, Vanderbilt University, Nashville, TN 37235, USA

[5]Vanderbilt Ingram Cancer Center, Vanderbilt Health, Nashville, TN 37232, USA

[6] Vanderbilt Institute of Chemical Biology, Vanderbilt University, Nashville, TN 37235, USA

[7]Department of Pathology, Microbiology, and Immunology, Vanderbilt Health, Nashville, TN 37232, USA

[8]Department of Medicine, Division of Rheumatology and Immunology, Vanderbilt Health, Nashville, TN 37232, USA

[9]Vanderbilt Center for Immunobiology, Vanderbilt Health, Nashville, TN 37232, USA

[10]Vanderbilt Institute for Infection, Immunology and Inflammation, Vanderbilt Health, Nashville, TN 37232, USA

[11]Department of Chemical and Biomolecular Engineering, The Ohio State University, Columbus, OH 43210, USA

*Corresponding Author: john.t.wilson@vanderbilt.edu

ABSTRACT

Cancer vaccines can generate tumor-specific T cells, but their efficacy against solid tumors is limited by an immunosuppressive tumor microenvironment (TME). To address this challenge, we developed nAlb-Vax, an albumin-binding nanobody vaccine platform designed to coordinate T cell priming in the lymphatic system with inflammatory remodeling of the TME. nAlb-Vax combines nanobody-fused peptide antigens with a nanobody-STING agonist conjugate as an adjuvant. Following subcutaneous (SC) administration, albumin binding enhanced antigen and adjuvant transport to draining lymph nodes (LNs), promoting antigen cross-presentation and antigen-presenting cell (APC) activation that elicited robust antigen-specific $CD8^+$ T cell responses. nAlb-Vax subsequently entered systemic circulation and preferentially accumulated within tumors, promoting an immunostimulatory TME that enhanced infiltration, proliferation, and function of vaccine-induced T cells. Therapeutic vaccination inhibited tumor growth and extended survival across multiple established murine solid tumor models, outperforming conventional vaccine technologies and generating durable immunity against multiple tumor-specific antigens (TSAs). These findings demonstrate that exploiting physiological albumin trafficking can coordinate lymphatic T cell priming with inflammatory TME remodeling to improve therapeutic cancer vaccination.

MAIN TEXT

INTRODUCTION

Cancer vaccines have long held promise for generating tumor antigen-specific cytotoxic T cells capable of selectively recognizing and eradicating cancer cells while establishing immune memory to prevent disease recurrence. Despite decades of largely disappointing clinical outcomes, recent advances in antigen discovery, tumor immunology, and precision medicine have renewed interest in cancer vaccines as a strategy to increase the magnitude, breadth, and durability of tumor-specific T cell responses[1,2], with recent clinical trials of personalized mRNA vaccines (intismeran autogene) demonstrating considerable promise in reducing the risk of melanoma recurrence[3–5].

Effective cancer vaccines aim to both prime naïve T cells and expand pre-existing memory T cells that recognize peptides derived from tumor-associated or tumor-specific antigens (TAAs or TSAs) presented on major histocompatibility complex (MHC) molecules[6–8]. To achieve this, tumor antigens must be delivered with appropriate adjuvants to promote antigen presentation by antigen-presenting cells (APCs) in an immunostimulatory context[2,9–12]. Cancer vaccine platforms primarily deliver tumor antigens as peptides or nucleic acid encoding tumor antigens[1]. While mRNA and DNA vaccines can possess intrinsic immunostimulatory properties, effective peptide vaccination requires spatiotemporal coordination of antigen and adjuvant delivery to APCs while overcoming the rapid clearance and poor cellular uptake characteristic of soluble peptide antigens[13,14]. Recent clinical trials in colorectal carcinoma (CRC), hepatocellular carcinoma (HCC), melanoma, lung cancer, renal cell carcinoma (RCC), and pancreatic ductal adenocarcinoma (PDAC) have demonstrated that peptide-based tumor antigen vaccines can elicit antitumor T cell responses with therapeutic benefit observed in some patients[15–21]. Despite this recent progress, the overall clinical efficacy of cancer vaccines remains modest, particularly in patients with advanced, metastatic, and/or immunologically ‘cold’ tumors with a highly immunosuppressive tumor microenvironment (TME).

Unlike prophylactic vaccines used to prevent infectious diseases, therapeutic cancer vaccines are administered in the context of established disease, where residual, unresectable, and/or metastatic tumors can impose substantial barriers to vaccine-induced immunity. The TME of solid tumors presents both biochemical and structural barriers to the infiltration and function of tumor-reactive T cells[22,23]. Tumor cells, fibroblasts, and immune cells can express inhibitory checkpoint ligands (e.g., PD-L1) and produce immunoregulatory cytokines and metabolites that suppress T cell function[22,23]. In addition, dysfunctional tumor vasculature can limit T cell infiltration and contribute to hypoxia that impairs T cell activity[24]. Indeed, it has been demonstrated that the adoptive transfer of supraphysiologic numbers of activated tumor antigen-specific $CD8^+$ T cells can fail to eradicate established solid tumors in both preclinical models and clinical settings[25–28]. This disconnect between the magnitude of peripheral vaccine-induced T cell response and antitumor activity may help explain why cancer vaccines that generate robust peripheral $CD8^+$ T cell responses often do not improve patient outcomes. Even when combined with immune checkpoint blockade (ICB) therapy (e.g., anti-PD-1, anti-PD-L1) most cancer

vaccine candidates have failed to meaningfully improve responses[29–31], underscoring the role of the immunosuppressive TME in limiting cancer vaccine efficacy. Consequently, many recent cancer vaccine clinical trials have focused on the adjuvant setting in patients with minimal residual disease, where lower tumor burden reduces barriers to vaccine-induced T cell function and the primary objective becomes prevention of disease recurrence[3,16,20,21,32,33].

Together, these observations suggest that effective therapeutic cancer vaccination may require not only robust priming of tumor antigen-specific T cells but also coordinated reprogramming of the TME into an inflamed, immunologically "hot" state that supports their infiltration, proliferation, and function[34,35]. Although vaccines are conventionally delivered via intramuscular (IM) or subcutaneous (SC) routes, emerging evidence suggests that intravenous (IV) administration can improve antitumor vaccine efficacy in some settings[36]. IV cancer vaccination is now being explored clinically using mRNA-encapsulating lipid nanoparticles (LNPs)[32,33,37], while nanoparticle assemblies of peptide antigens and Toll-like receptor 7/8 (TLR7/8) agonists are under preclinical development for IV vaccination[38,39]. While the mechanisms underlying improved responses remain incompletely understood, IV administration of vaccines can stimulate a systemic innate immune response capable of remodeling the TME and supporting T cell function. For example, IV administration of the personalized mRNA cancer vaccine autogene cevumeran induces a systemic cytokine response in patients[32], which preclinical studies have associated with enhanced antitumor response[40].

However, most cancer vaccine platforms have not been designed for delivery to tumors to reprogram the TME, and there is limited evidence that systemically administered vaccines substantially accumulate in human tumor tissue. Instead, IV-administered cancer vaccines primarily target APCs in the spleen to generate antitumor T cells[36,41]. While there is evidence that targeting vaccines to the spleen via IV vaccination can generate $CD8^+$ T cells with improved stem-like properties[38], it has also been observed that IV vaccination with nanoparticle vaccines generates fewer antigen-specific $CD8^+$ T cells than SC vaccination at equivalent doses[38,39]. This may result, in part, from suboptimal delivery to splenic APCs and/or accumulation in the liver, a tolerogenic organ that can restrict vaccine-mediated immune responses[42,43].

Together, these observations motivated us to develop a vaccine capable of addressing two spatially distinct requirements for effective antitumor immunity: robust T cell priming in lymphoid tissues and reprogramming the TME to enhance the infiltration and function of vaccine-induced T cells. Because most vaccines are not designed to efficiently distribute systemically and/or target tumors following local (SC or IM) injection, we sought to develop a cancer vaccine platform that could deliver peptide antigens and adjuvant to APCs in local draining lymph nodes (LNs) following SC injection while subsequently accessing the systemic circulation and tumor tissue. We hypothesized that the physiological trafficking of interstitial albumin through draining lymphatics and ultimately into the blood could provide a mechanism for distributing a SC-administered vaccine across both lymphoid and tumor compartments[44]. Albumin-binding strategies have previously been used to enhance delivery of vaccine cargoes to the injection site

draining LNs following SC administration, reflecting the efficient transport of albumin into lymphatic vessels and accumulation in lymphoid tissues[45–50]. Importantly, albumin can accumulate within tumors, where some cancers actively internalize albumin through micropinocytosis to support their increased metabolic and growth demands[51–53]. These properties have motivated the development of numerous therapeutic platforms that bind to and "hitchhike" on endogenous albumin to extend half-life and/or increase delivery to tumors[54–59].

In the context of cancer vaccines, albumin-binding lipids and small molecules such as Evans blue have been used to improve the lymphatic delivery of antigen and adjuvant to draining LNs and thereby enhance T cell priming[47,50]. However, lipophilic albumin-binding moieties can partition from albumin to increasingly hydrophobic interfaces such as cell membranes, potentially limiting their systemic bioavailability and tumor accumulation following SC administration[60]. We therefore sought to harness an albumin-binding nanobody (nAlb) to enable spatiotemporally coordinated delivery of antigen and adjuvant to both the draining LN and the TME. Nanobodies are small (~12-15 kDa), single chain proteins derived from the variable heavy chain (VHH) of camelid immunoglobulin Gs (IgGs) that can bind their targets with high specificity and affinity[61]. For example, nAlb binds albumin with a ~10-fold greater affinity than many commonly used lipophilic albumin-binding moieties and recognizes a defined epitope on albumin, thereby limiting nonspecific interactions while preserving FcRn-mediated albumin recycling that facilitates its long half-life[47,62,63]. We hypothesized that these pharmacological properties would enable nAlb to not only enhance the delivery of conjugated antigen and adjuvant cargoes to the local draining LN following SC administration but also facilitate access to systemic circulation and subsequent accumulation within tumors.

We previously developed a nanobody-drug conjugate (NDC) platform for the delivery of a diamidobenzimidazole (diABZI) agonist of the stimulator of interferon genes (STING) pathway. STING is a highly conserved, pattern recognition receptor and a central mediator of antitumor immunity[64]. STING activation promotes the expression of type-I interferons (IFN-I) and interferon-stimulated genes (ISGs), which have been attributed to enhanced antigen-specific $CD8^+$ T cell responses through potent APC activation, antigen cross-presentation, and inflammatory cytokine production[65–67]. Accordingly, STING agonists have been extensively investigated as cancer immunotherapies[68,69] and as adjuvants for therapeutic cancer vaccines[31,70–72]. We previously demonstrated that IV administration of an albumin-binding nanobody-diABZI conjugate (nAlb-diABZI) enriched STING activation at tumor sites, driving a remodeling of the TME that enhanced $CD8^+$ T cell infiltration and function and resulted in improved antitumor efficacy[62].

Here, we describe nAlb-Vax, a cancer vaccine platform designed to coordinate lymphoid T cell priming with tumor-localized innate immune activation following SC administration. nAlb-Vax combines peptide tumor antigens recombinantly fused to an albumin-binding nanobody (nAlb-antigen) with the albumin-binding nanobody-STING agonist conjugate nAlb-diABZI. We demonstrate that nAlb-Vax traffics to the local, injection site draining LN after SC administration

where it induces antigen presentation on MHC class I (MHC-I) by multiple APCs to generate an antigen-specific $CD8^+$ T cell response with antitumor function. When administered SC to tumor-bearing mice, we also found that nAlb-Vax enters systemic circulation and accumulates in the TME to enhance the infiltration of vaccine-induced $CD8^+$ T cells, resulting in superior antitumor efficacy compared to relevant controls. Collectively, these findings establish nAlb-Vax as a promising antigen-specific immunotherapy with the ability to both prime $CD8^+$ T cells in the lymphatics and distribute systemically to reprogram the TME, resulting in enhanced antitumor efficacy following localized vaccination.

RESULTS

Design and synthesis of albumin-binding nanobody vaccines

We previously demonstrated that the conjugation of the STING agonist diABZI to the C-terminus of nAlb extended serum half-life following IV administration relative to a non-albumin-binding control nanobody[62]. Because of the active and passive transport pathways that facilitate the lymphatic drainage and lymph node accumulation of albumin-bound cargoes[48], we hypothesized that this strategy could be extended to transporting diABZI and peptide antigens into the lymphatics following SC injection **(Fig. 1A)**. This transport phenomenon can be attributed to both the increase in effective molecular weight conferred by albumin (~67 kDa) binding, which raises albumin-bound cargoes above the ~20 kDa blood capillary cutoff to force lymphatic drainage[49], as well as active, endocytic transport by lymphatic endothelial cells through pathways involving the neonatal Fc receptor (FcRn), clathrin, and caveolin[73,74]. Previous computational modeling using RoseTTAFold and RosettaDock indicated that nAlb bound subdomain IIB of human serum albumin in a 1:1 ratio and did not compete with albumin binding to FcRn[62]. Using AlphaFold 3[75,76], we depicted nAlb binding mouse serum albumin (MSA) **(Fig. 1B)**, which bound with an affinity of ~1-10 nM as measured using biolayer interferometry (BLI) **(Fig. 1C)**.

To integrate peptide antigens at the C-terminus of nAlb (or other nanobodies which served as controls), we designed gene cassettes to express a fusion of the nanobody and peptide antigen linked by a flexible GGGS spacer. In this work, we utilized the peptide antigens $OVA_{251-270}$, a 20 amino acid peptide derived from the model antigen ovalbumin (OVA) that contains the H-2Kb-restricted epitope SIINFEKL, and $E7_{38-57}$, a 20 amino acid peptide derived from the human papillomavirus (HPV) E7 oncoprotein that contains the H-2Db-restricted epitope RAHYNIVTF. Downstream of the antigenic epitope, we placed a second GGGS spacer followed by a sortase ligation tag (LPETGG) for site-specific labeling with a Cy5 fluorophore for *in vivo* tracking and a hexahistidine tag (HHHHHH) to enable purification by immobilized metal affinity chromatography (IMAC). Following expression and purification, nanobody-antigen molecular weights were evaluated using electrospray ionization-mass spectrometry (ESI-MS) **(Fig. S1)** and we verified the maintenance of high albumin binding affinity for nAlb-antigen fusions using BLI **(Fig. S2)**.

To conjugate Cy5 or diABZI to nAlb or nAlb-antigen, an engineered pentamutant of sortase A (eSrtA) was used to site-selectively ligate amino-poly(ethylene glycol)$_3$-azide (NH_2-PEG_3-N_3) to the C-terminus of the nanobody to yield an azide-modified nanobody[77] that was subsequently conjugated to dibenzocyclooctyne (DBCO)-functionalized compounds via strain-promoted azide-alkyne cycloaddition (SPAAC) **(Fig. 1D)**. In this work, we used a DBCO-functionalized sulfo-Cy5 compound to label nanobodies for tracking purposes, and we used a DBCO-functionalized variant of diABZI linked via a PEG_{12} spacer for STING pathway agonism **(Fig. 1E)**[62]. Successful conjugation of payloads and conjugate purity were evaluated using ESI-MS **(Fig. S3)**. BLI analysis indicated that all nAlb conjugates maintained ~1-10 nM binding affinity to MSA **(Fig. S4)**.

Albumin-binding nanobody-antigen fusions accumulate in the local draining lymph node after subcutaneous administration

To determine if nAlb-antigen fusions accumulate in the injection-draining LN following SC administration, a fusion protein of nAlb and the model antigen $OVA_{251-270}$ (nAlb-$OVA_{251-270}$) was site-selectively labeled with a fluorescent dye (Cy5) for tracking (nAlb-$OVA_{251-270}$-Cy5). Mice were SC administered either a mixture of nAlb-$OVA_{251-270}$-Cy5 and nAlb-diABZI (nAlb-Vax-Cy5) or a mixture of a size-matched control nanobody-antigen fusion targeting GFP (nGFP-$OVA_{251-270}$-Cy5) and nAlb-diABZI (nGFP-Vax-Cy5) **(Fig. 1F)**. After 24 h, mice were euthanized and the draining LN (inguinal) was excised and imaged using an *in vivo* imaging system (IVIS). Fluorescent imaging using IVIS indicated that nAlb-mediated albumin-binding significantly increased the LN accumulation of Cy5-labeled peptide antigens compared to the GFP-binding control **(Fig. 1G-H)**, consistent with its small size (~15 kDa) and rapid clearance. Subsequently, draining inguinal LNs were processed for either immunofluorescent (IF) microscopy or flow cytometry to evaluate Cy5 uptake by individual immune cell populations. IF microscopy revealed Cy5 accumulation in the LN only with nAlb-Vax-Cy5 and indicated that the Cy5 signal was predominantly colocalized with macrophages ($F4/80^+$) and DCs ($CD11c^+$) **(Fig. 1I)**. This was supported by flow cytometric profiling of Cy5 association with major immune cell populations in the draining LN, finding that nAlb, but not nGFP, promoted uptake by phagocytic cells with antigen-presentation capabilities, including macrophages (MΦs; $CD11b^+F4/80^+$), granulocytes ($CD11b^+Gr\text{-}1^+$), and DCs ($CD11c^+$), corresponding to 55%, 40%, and 35% $Cy5^+$ cells within these respective populations **(Fig. 1J-K; Fig. S5)**. Collectively, these results demonstrate that fusion of peptide antigens to nAlb provides an effective platform for targeted antigen delivery to lymphatic APCs after SC injection for cancer vaccine applications.

nAlb-Vax induced STING activation drives antigen cross-presentation and co-stimulation to prime antigen-specific $CD8^+$ T cells

Effective cytotoxic $CD8^+$ T cell priming by APCs typically requires three signals. First, T cells recognize a peptide/MHC-I complex via a cognate T cell receptor (TCR). Second, the T cell co-stimulatory receptor CD28 binds its ligands CD80 and CD86 on activated APCs to amplify T

cell activation, proliferation, and survival. Third, inflammatory cytokine secretion by APCs directs T cell effector function and memory formation[78,79].

Activation of the STING pathway promotes the expression of IFN-Is and other proinflammatory cytokines to generate cytotoxic T lymphocytes[80]. Accordingly, we first sought to investigate the ability of nAlb-Vax to activate the STING pathway in MutuDC1940 cells, an immortalized conventional type 1 dendritic cell (cDC1; $CD8\alpha^+$) capable of cross-presenting antigen on MHC-I[81]. To test this, we treated cells with nAlb-Vax (the mixture of nAlb-$OVA_{251-270}$ and nAlb-diABZI) or nAlb-$OVA_{251-270}$ alone for 24 h. After 24 h, we collected the cell culture supernatants and performed enzyme-linked immunosorbent assays (ELISAs) to quantify the secretion of the STING-associated cytokines IFN-β and TNF-α. As expected, cytokine secretion was induced only by the full nAlb-Vax formulation containing nAlb-diABZI **(Fig. 2A-B)**, validating that nAlb-diABZI activates STING in cross-presenting DCs.

As STING-driven IFN-I signaling in DCs has been shown to license cross-presentation of exogenous antigens[82], we next sought to evaluate if nAlb-Vax could increase presentation of SIINFEKL ($OVA_{257-264}$) on MHC-I (H-2Kb) by MutuDC1940 cells. Again, cells were treated with nAlb-Vax or nAlb-$OVA_{251-270}$ alone for 24 h and peptide/MHC-I presentation was measured via flow cytometry by staining cells with a fluorescently labeled antibody that binds the SIINFEKL/H-2Kb complex. We found that MutuDC1940 cells most significantly cross-presented SIINFEKL following treatment with the full nAlb-Vax formulation containing nAlb-diABZI **(Fig. 2C; Fig. S6)**, suggesting that STING activation enhances antigen cross-presentation by DCs. Finally, as effective T cell priming also requires co-stimulation by APCs and STING activation is correlated with DC maturation and co-stimulatory molecule expression, we evaluated the ability of nAlb-Vax to induce expression of CD80 and CD86, finding that the nAlb-diABZI STING agonist was required for co-stimulation by MutuDC1940 cells **(Fig. 2D-E; Fig. S6)**. Additionally, since nAlb-Vax was efficiently delivered *in vivo* to additional types of APCs, including macrophages that are capable of antigen cross-presentation[83], we repeated these studies using primary bone marrow-derived macrophages (BMDMs) from C57BL/6 mice and observed similar results **(Fig. 2F-J; Fig. S7)**. Together, these data suggest that nAlb-diABZI can act as a potent cancer vaccine adjuvant through its ability to activate the STING pathway to induce antigen cross-presentation and co-stimulatory marker expression in both macrophages and DCs.

Having found that nAlb-Vax induced both antigen cross-presentation and co-stimulatory molecule expression by DCs and macrophages, we then sought to investigate whether these signals were temporally coordinated. To test this, we treated MutuDC1940 cells and BMDMs with nAlb-Vax for 0, 6, 12, 24, 48, and 72 h prior to quantifying the expression of H-2Kb/SIINFEKL, CD80, and CD86 by flow cytometry. We found that in both cell types CD86 expression peaked relatively quickly at around 12 h post-treatment and remained elevated for the duration of the study, while H-2Kb/SIINFEKL and CD80 expression began showing elevation around 12 h post-treatment and continued increasing until study termination **(Fig. 2K-L; Fig. S6; Fig. S7)**. These data are consistent with previous reports indicating that CD86 is often upregulated faster (often within 5-

12 h) and more robustly than CD80 (typically after 24 h)[84,85], and suggest that antigen cross-presentation and co-stimulation are temporally coordinated in both DCs and macrophages. STING-associated cytokines also remained elevated for the duration of the 72 h study **(Fig. S8)**. Additionally, we compared the level of SIINFEKL cross-presentation of nAlb-$OVA_{251-270}$ to equimolar amounts of full-length OVA by MutuDC1940 cells and BMDMs when adjuvanted with nAlb-diABZI via H-2Kb/SIINFEKL staining and flow cytometry. In both cell types, we observed that nAlb-Vax induced comparable, if not slightly higher, degrees of antigen cross-presentation compared to the mixture of OVA and nAlb-diABZI **(Fig. S9; Fig. S10; Fig. S11)**, suggesting that the sequence-level design of nAlb-$OVA_{251-270}$ allows for efficient processing and cross-presentation of the SIINFEKL epitope.

Having confirmed that nAlb-Vax can induce the required signals for effective T cell priming, we then treated MutuDC1940 cells with nAlb-Vax or nAlb-$OVA_{251-270}$ for 24 h prior to washing and co-culture with CellTrace Violet (CTV)-labeled OT-I T cells (primary, transgenic $CD8^+$ T cells with a TCR that recognizes H-2Kb/SIINFEKL) for an additional 72 h for analysis of proliferation and activation by flow cytometry. Analysis of CTV dilution indicated that OT-I T cells proliferated in response to nAlb-$OVA_{251-270}$ **(Fig. 2M; Fig. S12)**, with a higher frequency of proliferation and number of cell divisions in the presence of nAlb-diABZI **(Fig. 2M-N; Fig. S12)**. Additionally, we observed that nAlb-Vax most potently induced the upregulation of the activation marker CD69 by OT-I T cells **(Fig. 2O; Fig. S12)**. This supports the need for STING pathway activation to achieve antigen cross-presentation, co-stimulatory marker expression, and inflammatory cytokine secretion that together comprise the three-signal model of T cell priming.

Subcutaneous vaccination with nAlb-Vax generates antigen-specific $CD8^+$ T cells with an effector memory phenotype that are protective against tumor challenge

Having demonstrated that nAlb-Vax can induce antigen cross-presentation, co-stimulatory molecule expression, and inflammatory cytokine secretion that promoted antigen-specific T cell proliferation *in vitro*, we sought to test its capacity to generate an antitumor T cell response *in vivo*. C57BL/6 mice were vaccinated SC at the base of tail with a 1:1 molar ratio of 1.47 nmol (1.42 µg) of peptide antigen and 1.25 µg diABZI two times, 7 days apart. 7 days following the booster, the frequency of SIINFEKL-specific $CD8^+$ T cells among the peripheral blood mononuclear cells (PBMCs) was evaluated using H-2Kb/SIINFEKL tetramer staining. We first validated that including nAlb-diABZI as an adjuvant in the vaccine formulation was necessary to generate antigen-specific T cells, as mice treated with nAlb-$OVA_{251-270}$ alone failed to generate a response **(Fig. 3A; Fig. S13)**. We next evaluated the relative importance of lymphatic T cell priming in generating the T cell response by comparing the effects of SC vaccination to IV vaccination – which reduces distribution to the lymphatics and relies more on splenic T cell priming[36,38]. We found that compared to IV vaccination, SC vaccination generated ~3-fold more $tetramer^+$ $CD8^+$ T cells **(Fig. 3B; Fig. S14)**, which was consistent with previous reports using nanoparticle cancer vaccines[38,39], emphasizing the increased efficiency of lymphatic T cell priming in generating a peripheral $CD8^+$ T cell response.

Based on prior work demonstrating the importance of achieving spatiotemporally coordinated delivery of antigen and adjuvant to APCs in optimizing immune responses to vaccines[86], we next sought to evaluate if direct conjugation of diABZI to the nAlb-$OVA_{251-270}$ fusion (nAlb-$OVA_{251-270}$-diABZI) would impact the immunogenicity relative to a 1:1 mixture of nAlb-$OVA_{251-270}$ and nAlb-diABZI. To test this, we synthesized nAlb-$OVA_{251-270}$-diABZI using the same site-selective conjugation strategy used for the synthesis of nAlb-$OVA_{251-270}$-Cy5 **(Fig. S15)** and vaccinated mice with nAlb-Vax as a single molecule or a two-molecule mixture **(Fig. 3C)**. We observed that nAlb-Vax generated comparable tetramer responses when administered as a mixture or conjugate **(Fig. 3D; Fig. S16)**, suggesting that albumin-binding via nAlb allows for close matching of antigen and diABZI pharmacological properties to ensure co-delivery to individual APCs to achieve antigen-presentation in an inflammatory context *in vivo* even when administered as a two-molecule mixture. Based on this, we used a nAlb-Vax formulation comprising a mixture of nAlb-antigen and nAlb-diABZI for all subsequent investigations. This approach also offers the translational advantages of being able to independently control the dose and ratio of antigen and adjuvant components as well as using nAlb-diABZI as an off-the-shelf adjuvant that can be simply mixed with cocktails of nAlb-neoantigen fusions manufactured as a personalized vaccine product. We also sought to demonstrate that the enhanced lymphatic accumulation of both antigen and adjuvant achieved through albumin-binding was necessary to generate antigen-specific T cells. We found that adjuvanting nAlb-$OVA_{251-270}$ with small molecule diABZI instead of nAlb-diABZI or using an $OVA_{251-264}$ peptide instead of nAlb-$OVA_{251-270}$ both failed to generate a significant tetramer$^+$ $CD8^+$ T cell response **(Fig. 3D; Fig. S16)**. Collectively, these data show that albumin-binding via nAlb of both antigen and adjuvant is necessary to coordinate the lymphatic delivery of both vaccine components to achieve effective T cell priming.

We next sought to evaluate the phenotype and antitumor function of the nAlb-Vax-induced $CD8^+$ T cells. Mice were vaccinated two times, 7 days apart with nAlb-Vax or vehicle (PBS) control, blood was collected 7 days following the booster for analysis of the T cell response, and mice were challenged with an OVA-expressing B16.F10 melanoma cell line (B16.F10-OVA) 2 days following blood collection **(Fig. 3E)**[87]. Using flow cytometry, we quantified the magnitude of antigen-specific T cells generated via nAlb-Vax in peripheral blood **(Fig. 3F; Fig. S17)** and compared the phenotype of the vaccine-induced T cells to all $CD8^+$ T cells in the PBS control group, finding as expected that vaccine-induced T cells (tetramer$^+$$CD8\alpha^+$) exhibited an activated, proliferating (Ki-$67^+$$CD69^+$) phenotype **(Fig. 3G; Fig. S17)**. Additionally, we observed that nAlb-Vax induced a much stronger antigen-specific effector memory (T_{EM}; $CD44^+CD62L^-$) response compared to central memory (T_{CM}; $CD44^+CD62L^+$) response, with about 90% of the tetramer$^+$ T cells exhibiting a T_{EM} phenotype compared to only about 10% exhibiting a T_{CM} phenotype **(Fig. 3H; Fig. S17)**. This is notable as T_{EM} cells tend to be highly cytolytic with the ability to immediately recognize and kill target cells, which is important in generating antitumor immunity[88]. Following B16.F10-OVA tumor challenge, we observed that prophylactic vaccination with nAlb-Vax was able to significantly delay tumor growth compared to PBS control **(Fig. 3I-J; Fig. S18)**, confirming that nAlb-Vax-induced T cells have a capacity for antitumor function. We also

evaluated the long-term memory achieved through nAlb-Vax vaccination. Here, mice were vaccinated three times 45 days, 38 days, and 31 days prior to challenging mice with an OVA-expressing MC38 colorectal carcinoma cell line (MC38-OVA) **(Fig. 3K)**. Again, we observed that prophylactic vaccination with nAlb-Vax significantly inhibited tumor growth compared to PBS control **(Fig. 3L-M; Fig. S19)**, demonstrating that nAlb-Vax vaccination can generate long-lived antitumor immune memory.

Subcutaneously administered nAlb-Vax distributes systemically following initial lymphatic drainage and exhibits tumor tropism to deliver antigen and adjuvant to the TME

Given that effective cancer vaccines for advanced disease are likely to benefit from TME reprogramming that facilitates the infiltration and eradication of established tumors by vaccine-induced T cells, we hypothesized that the albumin hitchhiking capabilities of nAlb-Vax would enable systemic biodistribution following SC injection, potentially allowing both antigen and adjuvant to ultimately reach the TME. To test this hypothesis, we labeled both nAlb and nGFP with Cy5, administered nanobodies SC, and collected blood at defined timepoints through 24 h after administration to quantify the plasma concentration of Cy5 **(Fig. 4A)**. Both constructs exhibited pharmacokinetic (PK) profiles consistent with an SC administration route characterized by absorption and elimination phases. However, the maximum plasma concentration (C_{max}) was significantly higher for nAlb-Cy5 (171.4 nM) than for nGFP-Cy5 (14.6 nM), indicating that nAlb-mediated albumin hitchhiking enabled the conjugated Cy5 cargo to both enter and maintain systemic circulation following SC injection.

To determine if this ability to enter systemic circulation and extended half-life would lead to an increase in tumor accumulation, we inoculated mice with MC38 CRC tumors on the right flank, allowed the tumors to reach a size of ~200-300 mm^3, treated SC at the left base of tail with nAlb-Vax-Cy5 or nGFP-Vax-Cy5, and euthanized the mice after 24 h to analyze the organ distribution of Cy5 using fluorescent IVIS imaging and quantify the Cy5 uptake by major cell populations in the tumor and spleen using flow cytometry. IVIS imaging revealed that nAlb-Vax-Cy5 was predominantly detected in the tumor, consistent with our prior work[62], while nGFP-Vax-Cy5 was only detected in the kidneys, likely reflecting renal clearance of the low molecular weight nGFP-antigen fusion **(Fig. 4B-D)**. We then processed the tumors and spleens for flow cytometric profiling of Cy5 uptake by major cell populations and observed that nAlb-Vax-Cy5 was predominantly taken up by macrophages ($CD11b^+F4/80^+$), DCs ($CD11c^+$), endothelial cells ($CD45^-CD31^+$), and $CD45^-CD31^-$ cells (most likely cancer cells) in the tumor **(Fig. 4E-F; Fig. S20)** and by macrophages ($CD11b^+F4/80^+$), granulocytes ($CD11b^+Gr\text{-}1^+$), and DCs ($CD11c^+$) in the spleen **(Fig. S21A-B; Fig. S22)**. Collectively, these data demonstrate that nAlb-Vax enters systemic circulation following SC injection after first-pass lymphatic drainage, where it predominantly accumulates within the TME, suggesting that nAlb-Vax may be able to achieve both lymphatic T cell priming and potent TME reprogramming from a single SC injection. Additionally, the observed uptake of nAlb-Vax by APCs in the TME and spleen suggests that the

systemic biodistribution of nAlb-Vax may enable the reinvigoration of T cells primed in the local draining LN via antigen restimulation in peripheral lymphoid tissues and/or the TME.

Subcutaneous nAlb-Vax vaccination enhances antigen presentation by activated APCs in both the TME and secondary lymphoid tissues

Based on the ability of SC administered nAlb-Vax to deliver antigen and adjuvant to tumors and secondary lymphoid tissues, we next characterized APC activation and MHC-I antigen presentation in the injection-draining LN, spleen, and TME. We inoculated mice with MC38 tumors on the right flank, treated mice with ~200-300 mm^3 tumors with nAlb-Vax-Cy5 or PBS at the left base-of-tail, and euthanized mice 24 h later to profile the APCs in the injection-draining inguinal LN, spleen, and tumor using flow cytometry **(Fig. 5A)**. In these tissues, it was observed that nAlb-Vax treatment induced antigen cross-presentation (quantified via anti-H-2Kb/SIINFEKL staining) and co-stimulatory molecule (CD80 and CD86) expression on both macrophages and DCs. Additionally, we observed that treatment with nAlb-Vax increased the frequency of pro-inflammatory M1-like macrophages ($iNOS^+$) across all tissues and decreased the frequency of anti-inflammatory M2-like macrophages ($CD206^+Arg1^+$) in the injection-draining LN **(Fig. 5B; Fig. S23; Fig. S24; Fig. S25; Fig. S26; Fig. S27; Fig. S28; Fig. S29; Fig. S30)**.

To gain a deeper mechanistic understanding of how nAlb-Vax activates APCs, we used the Cy5 label on nAlb-Vax-Cy5 to identify APCs that endocytosed the antigen ($Cy5^+$) and those that did not take up the antigen ($Cy5^-$). In both populations, we evaluated the expression of CD80 and CD86 by DCs ($CD11c^+$) in the injection-draining LN **(Fig. 5C-D; Fig. S23; Fig. S24)** and tumor **(Fig. 5E-F; Fig. S27; Fig. S28)** and observed that while treatment with nAlb-Vax-Cy5 upregulated co-stimulatory molecule expression in both the $Cy5^+$ and $Cy5^-$ populations, levels (as measured by MFI) were increased in the $Cy5^+$ population over the $Cy5^-$ population. Similar trends were observed in macrophages ($CD11b^+F4/80^+$) in both the injection-draining LN **(Fig. 5G-H; Fig. S23; Fig. S24)** and tumor **(Fig. 5I-J; Fig. S27; Fig. S28)**. These data suggest that while direct uptake by APCs induces the most potent activation state, activated APCs are likely communicating with bystander APCs through the secretion of inflammatory cytokines. This is significant in the context of pro-inflammatory TME reprogramming, as direct STING activation and bystander inflammation should act in concert to enhance the infiltration of vaccine-induced T cells.

Finally, we examined the ability of nAlb-Vax to promote delivery of peptide antigen to cDC1s, a $CD8\alpha^+$ subset of DCs capable of efficiently cross-presenting antigens to induce antitumor cellular immunity[89]. Compared to conventional type 2 DCs (cDC2s; $CD8\alpha^-$), cDC1s internalized a similar amount of nAlb-$OVA_{251-270}$-Cy5 in both the injection-draining LN **(Fig. 5K; Fig. S23; Fig. S24)** and tumor **(Fig. 5M; Fig. S27; Fig. S28)**, indicating that nAlb-mediated antigen delivery was not preferential to either DC subtype. However, we observed that SIINFEKL presentation on H-2Kb was significantly upregulated by the cDC1 but not the cDC2 population in both the injection-draining LN **(Fig. 5L; Fig. S23; Fig. S24)** and tumor **(Fig. 5N; Fig. S27; Fig. S28)**, suggesting that cDC1s are the primary DC subset responsible for the cross-presentation of antigens delivered via nAlb-Vax.

Therapeutic vaccination with nAlb-Vax generates antigen-specific T cells with an activated, proliferating, effector memory phenotype in lymphoid tissues and the TME

STING activation in the TME can induce cancer antigen release and presentation in an immunostimulatory context that promotes endogenous priming and activation of antitumor T cells, a phenomenon often referred to as *in situ* vaccination[7,90]. We therefore sought to quantify and compare the phenotype of target antigen-specific $CD8^+$ T cells generated via treatment with nAlb-diABZI (*in situ* vaccination) or nAlb-Vax (*in situ* combined with antigen-targeted vaccination). To test this, we inoculated mice with MC38-OVA tumors on the right flank, allowed the tumors to reach a volume of ~100-150 mm^3, treated the mice two times 4 days apart, and then euthanized the mice 4 days following the second injection to quantify the antigen-specific T cells in the injection-draining LN, spleen, and tumor using H-2Kb/SIINFEKL tetramer staining **(Fig. 6A)**. In the injection-draining LN and spleen, we only observed a significant increase in the frequency of antigen-specific T cells compared to PBS control following treatment with nAlb-Vax **(Fig. 6B-C; Fig. S31; Fig. S32)**. In the tumor, however, we observed that both nAlb-diABZI and nAlb-Vax increased the frequency of antigen-specific T cells compared to PBS control, with nAlb-diABZI generating ~13% $tetramer^+$ T cells and nAlb-Vax generating ~20% $tetramer^+$ T cells of the entire $CD8^+$ T cell population **(Fig. 6D; Fig. S33)**. These data suggest that while STING activation in the TME via nAlb-diABZI can promote the priming and/or infiltration of endogenous antigen-specific T cells, nAlb-Vax is necessary to generate antigen-specific T cells in lymphoid tissues and augments the antigen-specific T cell response in the TME.

The strong T cell response elicited by nAlb-Vax in the MC38-OVA model resulted in a near complete regression of tumor growth **(Fig. S34A-C)** and therefore insufficient tissue for phenotyping of the tumor-infiltrating SIINFEKL-specific T cells. Accordingly, we repeated the study using an OVA-expressing YUMM1.7 murine melanoma tumor (YUMM-OVA) model. The YUMM1.7 melanoma line is derived from the $Braf^{V600E}Pten^{-/-}Cdkn2a^{-/-}$ genetically engineered mouse model and, unlike the MC38 line, expresses few tumor neoantigens and is poorly immunogenic and, therefore, provides a better model for investigating effects of SIINFEKL-specific $CD8^+$ T cells[91,92]. We inoculated mice with YUMM-OVA tumors on the right flank, allowed the tumors to reach a volume of ~100-150 mm^3, treated the mice three times 4 days apart, and then euthanized the mice 4 days following the third injection to quantify and phenotype the antigen-specific T cells present in the injection-draining LN, spleen, and tumor **(Fig. 6E)**. Using H-2Kb/SIINFEKL tetramer staining, we quantified the frequency of antigen-specific T cells in the injection site-draining LN, spleen, and tumor. As we found in the MC38-OVA model, we only observed significant increases in the frequency of antigen-specific $CD8^+$ T cells in the injection-draining LN and spleen following nAlb-Vax treatment, with slight trending increases following nAlb-diABZI monotherapy **(Fig. 6F-G; Fig. S35; Fig. S36; Fig. S37; Fig. S38)**. Interestingly, in YUMM-OVA tumors, we observed a relatively high frequency of ~30%, ~32%, and ~35% antigen-specific T cells in the PBS, nAlb-diABZI, and nAlb-Vax treatment groups **(Fig. 6H; Fig. S39; Fig. S40)**, respectively. We attribute this primarily to the infrequency of neoantigens in the parental YUMM1.7 cell line and the immunodominance of the OVA antigen in this model, where

it has been previously demonstrated that YUMM-OVA tumors generate endogenous T cell responses while parental YUMM1.7 tumors do not[92]. This therefore provides a model for evaluating the effect of nAlb-Vax on target antigen-specific T cell phenotype and function independent of tumor-infiltrating T cell density. In the injection-draining LN, tumor, and spleen, we observed that nAlb-Vax most significantly increased the frequency of activated, proliferating ($CD69^+Ki\text{-}67^+$) and proliferating, antigen-experienced ($Ki\text{-}67^+PD\text{-}1^+$) antigen-specific T cells – a phenotype that has been correlated with improved outcomes in patients[93] – compared to PBS control **(Fig. 6I; Fig. S34; Fig. S35; Fig. S36; Fig. S37; Fig. S38; Fig. S39; Fig. S40)**. Additionally, in the injection-draining LN and spleen, we observed that nAlb-Vax most significantly decreased the frequency of exhausted ($LAG\text{-}3^+TIM\text{-}3^+PD\text{-}1^+$) antigen-specific T cells and increased the frequency of T_{EM} ($CD44^+CD62L^-$) antigen-specific T cells compared to PBS control **(Fig. 6I; Fig. S35; Fig. S36; Fig. S37; Fig. S38; Fig. S39; Fig. S40; Fig. S41; Fig. S42)**. Moreover, in the TME, we observed that nAlb-Vax significantly increased the ratio of both $tetramer^+$:$CD4^+$ T cells and $CD8^+$:$CD4^+$ T cells, which have been used to prognosticate tumor responsiveness to immunotherapy[94,95], compared to both PBS and nAlb-diABZI controls **(Fig. 6J, K; Fig. S39)**.

Finally, to validate that the activated, proliferating, effector memory T cells generated through vaccination with nAlb-Vax could induce antitumor immunity, we inoculated mice with YUMM-OVA tumors on the right flank, allowed the tumors to reach a volume of ~100-150 mm^3, treated the mice three times 4 days apart using PBS, nAlb-diABZI, or nAlb-Vax, and monitored tumor growth until mice reached established endpoint criteria **(Fig. 6L)**. Compared to PBS and nAlb-diABZI controls, nAlb-Vax treatment most significantly inhibited tumor growth and extended mouse survival **(Fig. 6M-O; Fig. S43)**, suggesting that both the magnitude and phenotype of the antigen-specific T cell response induced by nAlb-Vax contribute to antitumor immunity.

Therapeutic vaccination with nAlb-Vax enhances antitumor immunity in multiple murine cancer models and outperforms clinical vaccine candidates

Having demonstrated that nAlb-Vax could induce antigen presentation, APC activation, antigen-specific $CD8^+$ T cell activation/proliferation, and antitumor immunity in a YUMM-OVA model of murine melanoma, we next sought to evaluate the efficacy of nAlb-Vax in a faster-growing, immunologically "cold" B16.F10-OVA model of melanoma that exhibits minimal T cell infiltration and is largely unresponsive to immunotherapy[87]. We inoculated mice with B16.F10-OVA tumors on the right flank, allowed the tumors to reach a volume of ~100-150 mm^3, treated the mice three times 4 days apart with nAlb-diABZI, nAlb-Vax, or PBS and monitored tumor growth until mice reached established endpoint criteria **(Fig. 7A)**. Compared to PBS and nAlb-diABZI controls, nAlb-Vax treatment most significantly inhibited tumor growth and extended mouse survival **(Fig. 7B-D; Fig. S44)**. Moreover, to emphasize the relative efficacy of nAlb-Vax in treating large, established, and poorly immunogenic solid tumors in preclinical mouse models, we compared the efficacy of nAlb-Vax to a vaccine comprising a mixture of peptide antigen

($OVA_{251-270}$) and the Toll-like receptor 3 (TLR3) agonist Poly(I:C) (pI:C), which mimics vaccine formulations that have been evaluated clinically[96]. Using the same B16.F10-OVA treatment timeline **(Fig. 7E)**, we observed that compared to PBS control, treatment with nAlb-Vax significantly inhibited tumor growth and extended survival, while treatment with $OVA_{251-270}$ peptide and pI:C adjuvant had no observable effect **(Fig. 7F-H; Fig. S45)**. Likewise, vaccination of mice bearing established (~100 mm^3) B16.F10-OVA tumors with OVA mRNA encapsulated in LNPs **(Fig. S46A)** failed to significantly inhibit tumor growth and extend survival **(Fig. S46B-F)**, highlighting the challenges in treating established B16.F10-OVA tumors with a clinically relevant mRNA vaccine formulation[32] and emphasizing the superior antitumor control achieved through nAlb-Vax vaccination.

Finally, we sought to demonstrate the applicability of nAlb-Vax beyond the $OVA_{251-270}$ model antigen by extending the platform to vaccination with a clinically relevant TSA. We redesigned nAlb-Vax to include the antigen $E7_{38-57}$, a 20 amino acid peptide derived from the HPV E7 oncoprotein that contains the H-2Db-restricted epitope RAHYNIVTF and demonstrated that MSA binding affinity was maintained using BLI **(Fig. S2B)**. We then inoculated mice on the right flank with TC-1 lung epithelial tumor cells which have been engineered to express the E6 and E7 oncoproteins that are produced by oncogenic strains of HPV and serve as the principal drivers of HPV-induced cancers. We allowed the TC-1 tumors to reach a volume of ~50-100 mm^3, treated the mice three times 4 days apart using PBS, nAlb-diABZI, or nAlb-Vax, collected PBMCs 4 days after the final treatment to analyze the antigen-specific T cell response, and monitored tumor growth until mice reached established endpoint criteria **(Fig. 7I)**. Using H-2Db/RAHYNIVTF tetramer staining, we determined that nAlb-Vax treatment significantly increased the frequency of circulating antigen-specific T cells compared to both PBS and nAlb-diABZI controls **(Fig. 7J; Fig. S47; Fig. S48)**. Moreover, immunophenotyping of the antigen-specific T cells induced following treatment indicated that nAlb-Vax treatment significantly increased the frequency of activated ($CD69^+$) antigen-specific T cells compared to PBS control **(Fig. 7K; Fig. S47; Fig. S48)** and significantly increased the frequency of proliferating (Ki-67^+) T cells compared to both PBS and nAlb-diABZI controls **(Fig. 7L; Fig. S47; Fig. S48)**. Similar to our findings using the $OVA_{251-270}$ antigen, $E7_{38-57}$-specific T cells exhibited a much stronger T_{EM} ($CD44^+CD62L^-$) than T_{CM} ($CD44^+CD62L^+$) phenotype at this timepoint **(Fig. 7M; Fig. S47; Fig. S48)**. While nAlb-diABZI significantly delayed tumor growth and extended survival compared to PBS control **(Fig. 7N-O; Fig. S49)**, all mice ultimately succumbed to disease **(Fig. 7Q)**. In striking contrast, treatment with nAlb-Vax significantly inhibited tumor growth and extended mouse survival compared to both PBS and nAlb-diABZI controls **(Fig. 7N-Q; Fig. S49)**, with all nAlb-Vax treated mice completely clearing their established tumors by Day 55 **(Fig. 7Q)**. To evaluate the durability of the antitumor immunity induced by nAlb-Vax, we re-challenged the surviving nAlb-Vax treated mice with TC-1 tumors on the contralateral (left) flank 90 days following the initial treatment **(Fig. 7I)**. Compared to an age-matched cohort of untreated (UT) mice, mice that had been previously vaccinated with nAlb-Vax exhibited significantly delayed tumor growth **(Fig. 7R-S, Fig. S50)**, with the majority of nAlb-Vax treated mice completely rejecting the tumor re-challenge.

Collectively, these data expand the applicability of nAlb-Vax to antigenic targets beyond OVA-derived model antigens and highlight the ability of nAlb-Vax to induce durable and complete antitumor immunity when targeting ubiquitous, oncogenic antigens, such as viral oncoproteins.

DISCUSSION

The immunosuppressive microenvironment of solid tumors presents a major barrier to the efficacy of virtually all T-cell based immunotherapies, including immune checkpoint inhibitors, adoptive T cell transfer therapy (e.g., TIL and CAR T), and cancer vaccines[22,23]. This barrier may help explain why cancer vaccines capable of generating robust peripheral antigen-specific T cell responses have not consistently translated into clinical benefit. Accordingly, recent clinical development of cancer vaccines has increasingly focused on patients with minimal residual disease following surgical resection, with the primary goal of preventing disease recurrence[3,16,20,21,32,33]. While early clinical trials are showing promise, this approach restricts the potential of cancer vaccines to a subset of patients. This motivates the need for cancer vaccine technologies that not only generate robust and durable tumor antigen-specific T cell responses but also reprogram the TME to enhance the infiltration and effector function of vaccine-induced T cells. Systemic (IV) administration of cancer vaccines has emerged as a promising strategy based, in part, on stimulating an adjuvant-driven systemic cytokine response with potential to remodel the TME[36,41]. This is exemplified clinically by mRNA/lipoplex vaccines (e.g., autogene cevumeran) that prime T cell responses in the spleen, while generating a systemic cytokine response[32,41]. However, IV vaccination has been demonstrated to generate fewer antigen-specific T cells than SC vaccination in preclinical models[38,39], and most vaccine platforms have not been designed to efficiently deliver immunostimulatory cargo to solid tumors to drive TME remodeling. This led us to postulate that an optimal cancer vaccine would be able to both traffic to the lymphatics to induce robust T cell priming and accumulate at tumor sites to locally inflame and reprogram the TME.

We designed nAlb-Vax based on the physiological trafficking of albumin from peripheral tissues through draining lymphatics and its subsequent systemic circulation and accumulation within solid tumors[45–50,54–59]. We hypothesized that an albumin-binding cancer vaccine could therefore enable access to both lymphoid and tumor compartments via a SC administration route, thereby coordinating lymphatic T cell priming and TME remodeling. We selected a nanobody-based albumin-binding domain (nAlb) due to its high selectivity and binding affinity, genetic programmability for installing diverse epitopes, established and scalable recombinant biomanufacturing workflows, and clinical precedent for use of similar albumin-binding nanobodies[97]. Consistent with this design rationale, we found that integration of antigen and the STING agonist adjuvant diABZI into nAlb-based constructs promoted their delivery to draining LNs and uptake by APCs, generating robust, antigen-specific $CD8^+$ T cell responses. Importantly, nAlb-Vax also accessed the systemic circulation following SC administration and accumulated within tumors where it activated STING and promoted inflammatory remodeling of the TME. This unique biodistribution profile enabled coordination of T cell priming and STING-driven TME reprogramming that enhanced vaccine efficacy across multiple established solid tumor models in

which conventional peptide or mRNA vaccine formulations exhibited little or no antitumor efficacy.

This transport behavior distinguishes nAlb-Vax from previously developed albumin-hitchhiking cancer vaccines based on lipophilic albumin-binding moieties, including the clinically investigated ELI-002 platform[16,19]. Lipophilic albumin binders efficiently promote lymphatic transport following SC administration but can partition from albumin into hydrophobic interfaces such as cell membranes, favoring lymphatic retention over systemic exposure and tumor accumulation[60]. By contrast, the selective and high-affinity interaction between nAlb and albumin enabled nAlb-Vax to retain the advantages of lymphatic delivery while also accessing systemic circulation to exploit albumin's inherent proclivity for tumor accumulation. While restricting vaccine exposure to lymphoid tissues may offer safety advantages[98], particularly for potent immunostimulatory adjuvants, clinical observations also underscore the challenge of therapeutic vaccination in patients with greater residual disease burden. Retrospective analysis of the AMPLIFY-7P trial in mutant KRAS (mKRAS)-driven PDAC suggested that a greater residual tumor burden was associated with worse clinical outcomes following ELI-002 vaccination[99], consistent with the broader challenge of achieving vaccine efficacy in the presence of established tumor-mediated immunosuppression. Although these observations do not establish that tumor-localized vaccine activity would overcome this limitation, they support continued investigation of vaccine strategies that couple efficient T cell priming with immune modulation at residual or established tumor sites.

Several limitations of our study warrant further investigation. First, we evaluated nAlb-Vax using only two MHC-I-restricted peptide antigens, and it remains unknown how broadly the platform can accommodate the chemically diverse antigenic sequences being explored clinically. Antigen sequence could influence recombinant production, construct stability, intracellular processing, and MHC-I presentation, and therefore systematic evaluation across a broader antigen repertoire will be important for establishing the generalizability of the nAlb-Vax platform. Similarly, the importance of $CD4^+$ T cells in cancer vaccine efficacy is increasingly clear[100], yet our study focused only on MHC-I-restricted $CD8^+$ T cell epitopes. Future studies incorporating MHC class II (MHC-II)-restricted helper epitopes or longer antigenic sequences will be required to determine how nAlb-Vax influences $CD4^+$ T cell immunity and whether $CD4^+$ T cell help further enhances the magnitude, durability, and antitumor activity of vaccine-induced $CD8^+$ T cell responses.

A second consideration is the therapeutic window associated with systemic exposure of innate immune agonists. We used the synthetic STING agonist diABZI as the nAlb-Vax adjuvant based on its capacity to enhance vaccine-induced $CD8^+$ T cell responses[71,72,101] and promote a multimodal remodeling of the TME[62,102,103]. Although we have previously demonstrated that IV-administered nAlb-diABZI is well-tolerated at the doses used here and preferentially enhances STING activation within tumors[62], treatment also induces transient elevations in serum cytokines with potential to constrain the therapeutic window. This is a challenge shared with current IV

administered cancer vaccines (e.g. mRNA/lipoplex vaccines) where elevated serum cytokine levels result in clinically manageable flu-like symptoms (e.g., fever, headache)[32,33,37]. Therefore, additional studies are necessary to define dosing and vaccination regimens that optimally balance nAlb-Vax immunogenicity, antitumor efficacy, and safety. Importantly, the modularity of the nAlb-Vax platform may provide opportunities to further control the magnitude and location of STING activation, including through modulation of albumin binding affinity or incorporation of environmentally cleavable linkers that regulate diABZI release within target tissues.

Finally, while our study demonstrated the importance of STING activation in the TME, the relative contribution of nAlb-Vax-mediated delivery of antigen within the TME remains unsolved. In addition to delivering nAlb-diABZI to tumors, nAlb-Vax delivers peptide antigen to the TME, where antigen is acquired and presented by tumor-infiltrating APCs and potentially tumor cells **(Fig. 4E, F; Fig. 5B; Fig. S29S, X)**. Such tumor-localized antigen delivery represents a mechanistically distinct feature of nAlb-Vax and raises the possibility that deposition of cognate antigen within tumors could promote local recognition, reactivation, or expansion of vaccine-induced T cells. Defining the extent to which this process contributes to therapeutic efficacy will be an important area for future investigation. More broadly, this mechanism suggests that nAlb-Vax-based tumor delivery of antigen and adjuvant could potentially complement vaccine platforms optimized for generating peripheral T cell responses. For example, nAlb-Vax could be explored as a tumor-directed booster following conventional vaccination (e.g., mRNA vaccines) to promote the recruitment and local reactivation of previously primed tumor antigen-specific T cells.

In summary, we have developed nAlb-Vax as a next-generation cancer vaccine technology that that leverages albumin-binding nanobodies as carriers to coordinate the delivery of tumor peptide antigens and immunostimulatory STING agonists across both lymphoid and tumor compartments. This unique vaccine biodistribution profile enables the priming of robust antitumor $CD8^+$ T cell responses in local injection site draining LNs while simultaneously inflaming and reprogramming the immunosuppressive microenvironment of distal tumors, thereby enhancing the infiltration and function of vaccine-induced T cells. Thus, nAlb-Vax represents a mechanistically and technologically distinct approach to cancer vaccine design with the potential to overcome barriers limiting the clinical efficacy of cancer vaccines, particularly for patients with residual or advanced disease.

MATERIALS AND METHODS

Cloning of Proteins

Gene cassettes were purchased from Integrated DNA Technologies in the form of a gene block, with cloning restriction sites placed on both flanking regions (BsaI–GGTCTC). To enable sortase-mediated bioconjugation of small molecules to nanobodies, a sortag motif was incorporated into the C-terminus of the nanobody sequence (LPETGGHHHHHHEPEA). The gene fragment was digested with BsaI-HF v2 in a Golden Gate master mix (New England Biolabs) and ligated into a pET28-b(+) plasmid. The construct was transformed into chemically competent

DH5α *E. coli* (New England Biolabs) and plated on Luria-Bertani agar with kanamycin. The sequence-verified pET28b plasmid was transformed into T7 Shuffle Express *E. coli* (New England Biolabs) for protein expression. Glycerol stocks of successfully transformed bacterial strains were maintained at −80 °C.

Expression and Purification of Proteins

Stabs of culture stocks (cloned into New England Biolabs T7 Shuffle Express *E. coli*) were added to culture tubes containing 5 mL Luria-Bertani broth (Gibco) with 50 µg/mL kanamycin (Research Products International) and incubated at 30 °C with shaking at 250 rpm for 16 h. Each culture tube was then transferred to a 2 L baffled flask containing 500 mL of 2xYT media (Fisher Scientific) with 50 µg/mL kanamycin and incubated at 30 °C with shaking at 250 rpm for 5-6 h until the OD600 reached ~0.8. The cultures were then cooled to 16 °C, and protein expression was induced via the addition of 0.5 mM isopropyl β-D-1-thiogalactopyranoside (IPTG) (Research Products International). Induced cultures were shaken overnight (~20-24 h) at 16 °C and 250 rpm. Bacteria were collected the following day via centrifugation at 3900 rpm for 10 min, and the pellet was resuspended in PBS containing 1 U/mL DNase I (New England Biolabs) and an EDTA-free protease inhibitor cocktail tablet (Roche). The cells were lysed by sonication in an ice bath for 5 s increments over 25 min. The resulting bacterial lysate was centrifuged at 12,000 rpm for 20 min to pellet cellular debris. The supernatant was added to a 50 mL Kontes Flex column (Kimbal Kontes Glassware) containing 5 mL of Ni-NTA resin (Thermo Fisher Scientific) that had been pre-equilibrated with PBS containing 10 mM imidazole (Research Products International) to limit nonspecific binding of the protein to the resin. The column was shaken at RT for 1 h, and then the supernatant was removed using gravity. Weakly bound proteins were removed from the resin by washing with PBS containing 20 mM imidazole until the A280 of the eluate was <0.2, followed by washing with PBS containing 50 mM imidazole until the A280 of the eluate was <0.2. Bound protein was then eluted from the resin using 15 mL of elution buffer (PBS containing 500 mM imidazole, pH 7.4). Endotoxin was removed using a Mustang® E (PES) 0.2 µm filter (Pall Corporation). The eluate was then concentrated to ~0.5 mL using a 15 mL 10 kDa MWCO Amicon centrifugal filter unit (MilliporeSigma) and subsequently purified via size exclusion chromatograph using an ÄKTA go™ fast performance liquid chromatography system (Cytiva) on a Hi-Load 16/60 Superdex 200 column using PBS, pH 7.4 as the running buffer at 4 °C. Purified fractions were pooled together and concentrated using a 15 mL 10 kDa MWCO Amicon centrifugal filter unit before storage at 4 °C (short-term) or -80 °C (long-term).

Following initial validation studies using novel constructs expressed and purified in house, validated protein constructs were subsequently ordered from GenScript using their proprietary TurboCHO™ Express Platform.

Engineered Sortase A (eSrtA) Sequence (No Start Codon)

eSrtA – HisTag

QAKPQIPKDKSKVAGYIEIPDADIKEPVYPGPATREQLNRGVSFAEENESLDDQNISIAGHT
FIDRPNYQFTNLKAAKKGSMVYFKVGNETRKYKMTSIRNVKPTAVEVLDEQKGKDKQL
TLITCDDYNEETGVWETRKIFVATEVKLE – HHHHHH

Formula: $C_{785}H_{1234}N_{220}O_{242}S_3$

Molecular Weight: 17721.94 Da

ε280 = 14440 M^{-1} cm^{-1}

Anti-Albumin (nAlb) Sequence (No Start Codon)

nAlb – Ligation Tag

EVQLVESGGGLVQPGGSLRLSCAASGFTFRSFGMSWVRQAPGKEPEWVSSISGSGSDTLY
ADSVKGRFTISRDNAKTTLYLQMNSLKPEDTAVYYCTIGGSLSRSSQGTQVTVSS –
LPETGGHHHHHHHEPEA

Formula: $C_{606}H_{939}N_{175}O_{198}S_4$

Molecular Weight: 13972.42 Da

ε280 = 17085 M^{-1} cm^{-1}

Anti-GFP (nGFP) Sequence (No Start Codon)

nGFP – Ligation Tag

MQVQLQESGGALVQPGGSLRLSCAASGFPVNRYSMRWYRQAPGKEREWVAGMSSAGD
RSSYEDSVKGRFTISRDDARNTVYLQMNSLKPEDTAVYYCNVNVGFEYWGQGTQVTVS
S – LPETGGHHHHHHHEPEA

Formula: $C_{636}H_{964}N_{190}O_{201}S_6$

Molecular Weight: 14680.16 Da

ε280 = 27055 M^{-1} cm^{-1}

Anti-Albumin-OVA$_{251-270}$ (nAlb-OVA$_{251-270}$) Sequence (No Start Codon)

nAlb-OVA$_{251-270}$ – Ligation Tag

EVQLVESGGGLVQPGGSLRLSCAASGFTFRSFGMSWVRQAPGKEPEWVSSISGSGSDTLY
ADSVKGRFTISRDNAKTTLYLQMNSLKPEDTAVYYCTIGGSLSRSSQGTQVTVSS –
GGGSGLEQLESIINFEKLTEWTSSGGGS – LPETGGHHHHHHHEPEA

Formula: $C_{728}H_{1127}N_{207}O_{243}S_4$

Molecular Weight: 16795.44 Da

ε280 = 22585 M^{-1} cm^{-1}

Anti-GFP-OVA$_{251-270}$ (nGFP-OVA$_{251-270}$) Sequence (No Start Codon)

nGFP-OVA$_{251-270}$ – Ligation Tag

MQVQLQESGGALVQPGGSLRLSCAASGFPVNRYSMRWYRQAPGKEREWVAGMSSAGD
RSSYEDSVKGRFTISRDDARNTVYLQMNSLKPEDTAVYYCNVNVGFEYWGQGTQVTVS
S – GGGSGLEQLESIINFEKLTEWTSSGGGS – LPETGGHHHHHHHEPEA

Formula: $C_{758}H_{1152}N_{222}O_{246}S_6$

Molecular Weight: 17503.19 Da

ε280 = 32555 M^{-1} cm^{-1}

Anti-Albumin-E7$_{38-57}$ (nAlb-E7$_{38-57}$) Sequence (No Start Codon)

nAlb-E7$_{38-57}$ – Ligation Tag

EVQLVESGGGLVQPGGSLRLSCAASGFTFRSFGMSWVRQAPGKEPEWVSSISGSGSDTLY
ADSVKGRFTISRDNAKTTLYLQMNSLKPEDTAVYYCTIGGSLSRSSQGTQVTVSS –
GGGSIDGPAGQAEPDRAHYNIVTFGGGS – LPETGGHHHHHHHEPEA

Formula: $C_{720}H_{1108}N_{210}O_{238}S_4$

Molecular Weight: 16642.22 Da

ε280 = 18575 M^{-1} cm^{-1}

Computational Modeling of Proteins

nAlb and MSA were modeled *in silico* using AlphaFold 3 [75,76] (Google DeepMind). The best fit structures of nAlb and the nAlb/MSA complex were exported to PyMOL (version 3.1.4.1) to generate figures of the structures.

Biolayer Interferometry

Biotinylated MSA (ACROBiosystems) was dissolved in BLI buffer (10 mM HEPES, 3 mM EDTA, 150 mM NaCl, 0.01% Tween 20) at 1 μg/mL and nanobodies were buffer exchanged to BLI buffer using 15 mL 10 kDa MWCO Amicon centrifugal filter units. Octet® Streptavidin (SA) Biosensors (Sartorius) were incubated in 1 μg/mL biotinylated MSA for 300 s at 1000 rpm to load the sensor tip using an Octet® R8, 8-Channel Protein Analysis System (Sartorius), followed by rinsing in BLI buffer for 60 s at 1000 rpm to remove excess MSA from the sensor tips. MSA-loaded sensor tips were then incubated in a 2-fold dilution series of indicated nanobodies for 500 s at 1000 rpm to facilitate nanobody association, followed by rinsing in BLI buffer for 500 s at 1000 rpm to permit nanobody dissociation. Data was fit to a 1:1 binding model using the Octet® Analysis Studio Software (Sartorius) to determine the affinity constant (K_d) of the indicated nanobody.

Synthesis of DBCO-PEG$_{12}$-diABZI

DBCO-PEG$_{12}$-diABZI was synthesized and characterized as described previously[62].

Enzymatic Bioconjugation and SPAAC Reactions

For sortase-mediated ligation of azido-PEG$_3$-amine (N_3-PEG$_3$-NH_2) (BroadPharm) to the C-terminus of nanobodies, nanobodies (250 μM) were combined with an engineered pentamutant of sortase A (eSrtA)[77] (12.5 μM) and N_3-PEG$_3$-NH_2 (20 mM) in eSrtA reaction buffer (50 mM Tris, 150 mM NaCl, 10 mM $CaCl_2$, pH 7.4) and mixed with a rotary shaker for 2 h at RT. The reaction mixture was buffer exchanged to PBS and added to a 20 mL Kontes Flex column (Kimbal Kontes Glassware) containing 2.5 mL of Ni-NTA resin (Thermo Fisher Scientific) that had been pre-equilibrated with PBS and shaken at RT for 30-60 minutes. Unbound protein (nanobody-azide conjugates) was collected via elution using PBS, while unreacted nanobodies (containing the LPETGGHHHHHHEPEA C-terminal motif), the cleaved sortag (GGHHHHHHEPEA), and eSrtA (containing a 6xHisTag) remained bound to the Ni-NTA resin. Purified nanobody-azide conjugates were buffer exchanged to PBS and concentrated using 15 mL 10 kDa MWCO Amicon centrifugal filter units (MilliporeSigma). For nanobodies containing histidine residues in their native sequences, proteins were eluted using PBS containing 10 mM imidazole (Research Products International) and subsequently buffer exchanged to PBS and concentrated using 15 mL 10 kDa MWCO Amicon centrifugal filter units. Strain promoted azide-alkyne cycloaddition (SPAAC) reactions were performed by incubating nanobody-azide conjugates with 5x molar excess DBCO-PEG$_{12}$-diABZI at 37 °C for 6 h or 2.5x molar excess sulfo-Cy5-DBCO (BroadPharm) at RT for 6 h. Following completion of the reactions, final products were purified using 7 kDa MWCO 10 mL Zeba Spin Desalting Columns (Thermo Fisher Scientific) according to the manufacturer's instructions. Successful reaction completion and purity was verified by ESI-MS.

ESI-MS

Proteins were buffer exchanged into 200 mM ammonium acetate ($NH_4C_2H_3O_2$), pH 5.5, and concentrated to approximately 100 μM. Raw mass spectra data was collected using an Agilent 6560A ion mobility time-of-flight (TOF) mass spectrometer at a range of 50-20,000 *m/z* over a period of 2 min. Data were analyzed with Agilent MassHunter IM-MS Browser (version 10.0) to reveal *m/z* data, where files were condensed across the 2 min run. These *m/z* data were deconvoluted using UniDec (version 7.0.2)[104] to provide the deconvoluted mass spectra using background subtraction in a range of 1000-5000 *m/z* and with an export range of 5000-50000 Da.

Animal Care and Ethics Declaration

All studies using animals, including surgical and experimental procedures, were completed under an Animal Care Protocol (M2200023) approved by the Vanderbilt University Institutional Animal Care and Use Committee (IACUC). Animal health assessments were completed using standard operating procedures approved by Vanderbilt University IACUC.

Ex Vivo Imaging Experiments

6-8 weeks old female C57Bl/6j mice (The Jackson Laboratory) were treated SC at the left base-of-tail with 5 nmol Cy5-labeled nanobody-antigen fusion and 1.25 µg nAlb-diABZI. Mice were euthanized via CO_2 asphyxiation 24 h post treatment. Injection-draining inguinal LNs, tumors, and major clearance organs (livers, lungs, kidneys, heart, spleen) were excised, rinsed in PBS, and transferred to the stage of an IVIS Lumina III In Vivo Imaging System (IVIS) (Revvity). Cy5 radiant efficiency (fluorescence) was measured, and the average radiant efficiency per cm^2 of each organ was determined by manually drawing regions of interest (ROIs) around each organ using the Living Image® software (Revvity, version 4.8.2). ROI measurements were normalized to account for autofluorescence by subtracting out the average radiant efficiency of each organ/tissue in the PBS group.

Immunofluorescent Confocal Microscopy

6-8 weeks old female C57Bl/6j mice (The Jackson Laboratory) were treated SC at the left base-of-tail with 5 nmol Cy5-labeled nanobody-antigen fusion and 1.25 µg nAlb-diABZI. Mice were euthanized via CO_2 asphyxiation 24 h post treatment. Injection-draining inguinal LNs were excised, rinsed in PBS, and placed in histology cassettes (Fisher Scientific). Cassettes were placed in 4% paraformaldehyde (PFA) (Thermo Fisher Scientific) in PBS and incubated at 4 °C with gentle rocking for 3-4 h. Cassettes were then washed once with PBS and further incubated in 30% sucrose (Thermo Fisher Scientific) in PBS with gentle rocking for 72 h at 4 °C. Following incubation, LNs were removed from cassettes and embedded in Tissue-Tek O.C.T. Compound (Sakura Finetek USA) within Peel-A-Way™ embedding molds (Millipore Sigma) and flash frozen in liquid nitrogen (LN_2). Frozen samples were stored at -80 °C until sectioning.

Confocal imaging was performed as previously described[105]. Briefly, frozen tissues were first sliced utilizing the Leica Cryostat CM1850 into 10 µm sections. Tissue sections were then rehydrated with wash buffer (1X PBS containing 0.5% Tween 20 (Sigma)). Blocking buffer (1X PBS containing 2% bovine serum albumin (Jackson ImmunoResearch) and 10% normal goat serum (Sigma Aldrich)) was placed onto tissues for 60-120 min at RT to minimize non-specific binding of primary and secondary antibodies. Tissues were then washed and incubated with a Streptavidin/Biotin blocking kit (Vector Laboratories) according to the manufacturer's instructions. Following this, tissues were incubated in permeabilization buffer (1X PBS containing 2% Triton X-100 (Sigma Aldrich)) for 30 min at RT. Tissues were then washed and incubated with the primary antibody cocktail listed in **Table S1** for 60-120 min. Tissues were then washed with wash buffer and incubated with the secondary antibody cocktail listen in **Table S1** for 60-120 min. Slides were again washed with wash buffer and then mounted with mounting medium (ProLong Gold Antifade Mountant). Images were acquired on the Zeiss LSM780 via the 10X or 20X 0.9 NA Plan Apo. Images were pseudocolored and overlaid using Imaris Microscopy Image Analysis Software (Oxford Instruments, version 11.0).

Flow Cytometry of Lymph Nodes

6-8 weeks old female C57Bl/6j mice (The Jackson Laboratory) were treated SC at the left base-of-tail with indicated nanobody-antigen fusion and/or 1.25 µg nAlb-diABZI. Mice were euthanized via CO_2 asphyxiation at indicated timepoints. Injection-draining inguinal LNs were excised, rinsed in PBS, and transferred to a 70 µm cell strainer (Fisher Scientific) where they were mashed into a single cell suspension. Cells were rinsed in flow buffer (PBS containing 2% FBS) followed by incubation in tetramer if applicable for 2 h at 4 °C, followed by Fc-block (anti-mouse CD16/CD32, Cytek Biosciences) for 15 min at 4 °C. Cells were then stained with indicated antibodies for 30 min at 4 °C, rinsed with flow buffer, fixed with 2% paraformaldehyde (PFA) in PBS (Thermo Fisher Scientific), rinsed with flow buffer again, and resuspended in 100 uL flow buffer for analysis. For cells analyzed using panels containing intracellular markers, instead of fixing with 2% PFA, cells were fixed using fixation solution from a eBioscience™ Foxp3 / Transcription Factor Fixation/Permeabilization Concentrate and Diluent kit (ThermoFisher) and stained with intracellular antibodies for an additional 30 min at RT prior to rinsing and resuspending in 100 uL flow buffer for analysis. Data was collected using a Cytek Northern Lights multispectral flow cytometer and analyzed using FlowJo (BD Biosciences, version 10.10.0).

Cell Culture

MutuDC1940s were a gift from Dr. Denis Mogilenko and were maintained in Iscove's Modified Dulbecco's Medium (IMDM, Gibco) supplemented with 10% heat inactivated FBS (Gibco), 100 U/mL penicillin (Gibco), 100 µg/mL streptomycin (Gibco), 2 mM L-glutamine (Gibco), 1X GlutaMAX (Gibco), 25 mM HEPES, 1 mM sodium pyruvate (Gibco), and 50 µM β-mercaptoethanol (Sigma Aldrich). Cells were passaged when confluency reached 70–90% using CellStripper™ non-enzymatic cell dissociation solution (Corning). B16.F10-OVA cells were a gift from Dr. Amanda Lund and were maintained in Dulbecco's modified Eagle's medium (DMEM, Gibco) supplemented with 4.5 g/L D-glucose, 10% heat inactivated FBS (Gibco), 100 U/mL penicillin (Gibco), 100 µg/mL streptomycin (Gibco), 2 mM L-glutamine (Gibco), 25 mM HEPES, 1 mM sodium pyruvate (Gibco), and 1X nonessential amino acids (Corning). OVA expression was maintained through continuous selection using 390 µg/mL G418 sulfate (geneticin, Corning) after every passage. Cells were passaged when confluency reached 70–90% using 0.25% trypsin-EDTA (Gibco). MC38-OVA cells were maintained in Dulbecco's modified Eagle's medium (DMEM, Gibco) supplemented with 4.5 g/L D-glucose, 10% heat inactivated FBS (Gibco), 100 U/mL penicillin (Gibco), 100 µg/mL streptomycin (Gibco), 2 mM L-glutamine (Gibco), 25 mM HEPES, 1 mM sodium pyruvate (Gibco), and 1X nonessential amino acids (Corning). OVA expression was maintained through continuous selection using 10 µg/mL puromycin (ThermoFisher) after every passage. Cells were passaged when confluency reached 70–90% using 0.25% trypsin-EDTA (Gibco). Parental MC38 cells (ATCC) were maintained in Dulbecco's modified Eagle's medium (DMEM, Gibco) supplemented with 4.5 g/L D-glucose, 10% heat inactivated FBS (Gibco), 100 U/mL penicillin (Gibco), 100 µg/mL streptomycin (Gibco), 2 mM L-glutamine (Gibco), 25 mM HEPES, 1 mM sodium pyruvate (Gibco), and 1X nonessential amino acids (Corning). Cells were passaged when confluency reached 70–90% using 0.25% trypsin-EDTA (Gibco). YUMM-OVA

cells were a gift from Dr. Amanda Lund and were maintained in 1:1 Dulbecco's modified Eagle's medium (DMEM, Gibco) and Ham's F-12 nutrient mixture (F12, Gibco) supplemented with 10% heat inactivated FBS (Gibco), 100 U/mL penicillin (Gibco), 100 µg/mL streptomycin (Gibco), 2 mM L-glutamine (Gibco), 15 mM HEPES, and 1X nonessential amino acids (Corning). OVA expression was maintained through continuous selection using 0.5 µg/mL puromycin (ThermoFisher) after every passage. Cells were passaged when confluency reached 70–90% using 0.25% trypsin-EDTA (Gibco). TC-1 cells (Cytion) were maintained in Dulbecco's modified Eagle's medium (DMEM, Gibco) supplemented with 4.5 g/L D-glucose, 10% heat inactivated FBS (Gibco), 100 U/mL penicillin (Gibco), 100 µg/mL streptomycin (Gibco), 2 mM L-glutamine (Gibco), 25 mM HEPES, 1 mM sodium pyruvate (Gibco), and 3.7 g/L $NaHCO_3$ (Research Products International). Cells were passaged when confluency reached 70–90% using StemPro™ Accutase™ (Gibco). Primary BMDMs were isolated from the femurs and tibias of 5-10 weeks old C57Bl/6j mice (The Jackson Laboratory) following CO_2 asphyxiation. In brief, bone marrow was passed through a 70 µm cell strainer (Fisher Scientific) to create a single cell suspension, treated with ACK Lysing Buffer (KD Medical) for 5 min to remove erythrocytes, and seeded in 10 mL of complete BMDM media (RPMI 1640 supplemented with 10% heat inactivated FBS (Gibco), 100 U/mL penicillin (Gibco), 100 µg/mL streptomycin (Gibco), 2 mM L-glutamine (Gibco), 10 mM HEPES (Gibco), 1 mM sodium pyruvate (Gibco), 1X nonessential amino acids (Corning), and 55 µM β-mercaptoethanol (Sigma Aldrich)) in a 100 x 15 mm polystyrene petri dish (VWR) at a density of 4-5 million cells/dish. To force differentiation into BMDMs, 20 ng/mL macrophage colony-stimulating factor (M-CSF, PeproTech) was added to the media, and media was refreshed on days 3 and 5 post cell isolation. Beginning on day 7, and repeating every other day thereafter, media was refreshed using only 10 ng/mL M-CSF. Cells were used for experiments between days 8-12 and discarded after day 12. All cells were maintained at 37 °C in 5% CO_2.

MutuDC1940/BMDM Maturation and Activation

MutuDC1940s were seeded on 12 well tissue culture treated plates, and BMDMs were seeded on 12 well non-tissue culture treated plates, both at a density of 500,000 cells/well, and cultured overnight prior to treatment. Cells were treated with 0.25 µM of nAlb-$OVA_{251-270}$, nAlb-diABZI, and/or OVA protein (InvivoGen) for 24 h unless otherwise indicated. Following treatment, supernatants were collected for ELISA analysis and cells were collected for flow cytometric analysis.

Flow Cytometry of *In Vitro* STING Activation

Following treatment, cells were scraped into media using Cell Lifters (Corning) and transferred to 1.5 mL microcentrifuge tubes. Cells were centrifuged at 400 x g for 5 min to pellet. The top 80-90% of media was aspirated, and cells were transferred to 96 well round bottom plates (ThermoFisher) for processing. Cells were rinsed in flow buffer (PBS containing 2% FBS) followed by incubation in Fc-block (anti-mouse CD16/CD32, Cytek Biosciences) for 15 min at 4 °C. Cells were then stained with indicated antibodies for 30 min at 4 °C, rinsed with flow buffer,

fixed with 2% paraformaldehyde (PFA) in PBS (Thermo Fisher Scientific), rinsed with flow buffer again, and resuspended in 100 uL flow buffer for analysis. Data was collected using a Cytek Northern Lights multispectral flow cytometer and analyzed using FlowJo (BD Biosciences, version 10.10.0). Normalized relative expression was calculated as:

$$\textbf{Normalized Relative Expression} = \frac{MFI_{Sample} - Avg(MFI_{PBS})}{Avg(MFI_{MAX}) - Avg(MFI_{PBS})}$$

Where MFI_{MAX} is the MFI at the timepoint in which the maximum expression of each marker occurred, and MFI_{PBS} is the MFI of the vehicle treated group.

ELISA Analysis of Cell Culture Supernatants

Following treatment, cell culture supernatants were collected in 1.5 mL microcentrifuge tubes and centrifuged at 2000 x g for 10 min to pellet cell debris. The top 80-90% of the supernatant was transferred to another 1.5 mL microcentrifuge tube and stored at -80 °C until analysis. For murine interferon-β (mIFN-β) ELISA, supernatants were processed using a LumiKine™ Xpress mIFN-β 2.0 ELISA kit (InvivoGen) according to the manufacturer's instructions. For murine tumor necrosis factor-α (mTNF-α) ELISA, supernatants were processed using a Mouse TNF alpha ELISA Kit (Invitrogen) according to the manufacturer's instructions. Luminescence and absorbance measurements were made using a Synergy HI plate reader (Bio-Tek).

OT-I T Cell Isolation and Co-Culture with MutuDC1940s

MutuDC1940 cells were seeded in 96 well round bottom plates (ThermoFisher) at a density of 25,000 cells/well and cultured overnight. Cells were then treated with vehicle (media) or 0.25 μM nAlb-$OVA_{251-270}$ and/or nAlb-diABZI for 24 h. Following 24 h, media was refreshed and 50,000 CellTrace™ Violet (CTV, ThermoFisher)-labeled OT-I T Cells were added to each well and cultured for 72 h. Following 72 h co-culture, OT-I T cells were collected and analyzed via flow cytometry. OT-I T cells were isolated and labeled with CellTrace™ Violet as follows: 6-8 weeks old female C57BL/6-Tg(TcraTcrb)1100Mjb/J (OT-I) transgenic mice (The Jackson Laboratory) were asphyxiated using CO_2 and spleens were isolated and transferred to 70 μm cell strainers (Fisher Scientific) and mashed into a single cell suspension. The flowthrough was centrifuged at 380 x g for 5 min and splenocytes were resuspended in 3 mL ACK Lysing Buffer (KD Medical) for 5 min to remove erythrocytes. Following erythrocyte removal, $CD8^+$ T cells were extracted using an EasySep™ Mouse $CD8^+$ T Cell Isolation Kit (STEMCELL Technologies) according to the manufacturer's instructions. Isolated OT-I $CD8^+$ T Cells were resuspended in 1 μM CellTrace™ Violet (CTV, ThermoFisher) in PBS at $2x10^6$ cells/mL and placed in an incubator for 20 min to stain, mixing with a pipette after the first 10 min. Following staining, cells were diluted 5x in media to quench the reaction, centrifuged at 380 x g for 5 min to pellet cells, and resuspended in media ahead of co-culture with mutuDC1940s.

Flow Cytometry of OT-I T Cells

OT-I T cells were collected with a pipette and transferred to 96 well round bottom plates (ThermoFisher) for processing. Cells were rinsed in flow buffer (PBS containing 2% FBS) followed by incubation in Fc-block (anti-mouse CD16/CD32, Cytek Biosciences) for 15 min at 4 °C. Cells were then stained with indicated antibodies for 30 min at 4 °C, rinsed with flow buffer, fixed with 2% paraformaldehyde (PFA) in PBS (Thermo Fisher Scientific), rinsed with flow buffer again, and resuspended in 100 uL flow buffer for analysis. Data was collected using a Cytek Northern Lights multispectral flow cytometer and analyzed using FlowJo (BD Biosciences, version 10.10.0).

Flow Cytometry of PBMCs

6-8 weeks old female C57Bl/6j mice (The Jackson Laboratory) were treated with indicated constructs (1.47 nmol nAlb-$OVA_{251-270}$, 5.88 nmol nAlb-$OVA_{251-270}$, 1.25 µg nAlb-diABZI, 1.25 µg diABZI (Selleck Chemicals), 1.47 nmol $OVA_{251-264}$ peptide (GenScript), and/or 5.88 nmol nAlb-$E7_{38-57}$) at indicated timepoints. On the day of analysis, blood was collected via cheek bleeds and processed for flow cytometric analysis of peripheral blood mononuclear cells (PBMCs). Erythrocytes were removed by incubating blood in 5 mL ACK Lysing Buffer (KD Medical) for 5 min two times. PBMCs were rinsed in flow buffer (PBS containing 2% FBS) followed by incubation in tetramer for 2 h at 4 °C, followed by Fc-block (anti-mouse CD16/CD32, Cytek Biosciences) for 15 min at 4 °C. PBMCs were then stained with indicated antibodies for 30 min at 4 °C, rinsed with flow buffer, fixed with 2% paraformaldehyde (PFA) in PBS (Thermo Fisher Scientific), rinsed with flow buffer again, and resuspended in 100 uL flow buffer for analysis. For cells analyzed using panels containing intracellular markers, instead of fixing with 2% PFA, cells were fixed using fixation solution from a eBioscience™ Foxp3 / Transcription Factor Fixation/Permeabilization Concentrate and Diluent kit (ThermoFisher) and stained with intracellular antibodies for an additional 30 min at RT prior to rinsing and resuspending in 100 uL flow buffer for analysis. Data was collected using a Cytek® Amnis® CellStream® Flow Cytometer for **Fig. 3A, D** and a Cytek Northern Lights multispectral flow cytometer for **Fig. 3B, Fig. 3F-H, and Fig. 7J-M** and analyzed using FlowJo (BD Biosciences, version 10.10.0).

Prophylactic Tumor Models

6-8 weeks old female C57Bl/6j mice (The Jackson Laboratory) were treated with indicated constructs (PBS, 1.47 nmol nAlb-$OVA_{251-270}$, 5.88 nmol nAlb-$OVA_{251-270}$, and/or 1.25 µg nAlb-diABZI) two times seven days apart for B16.F10-OVA challenge and three times seven days apart for MC38-OVA challenge. Nine days following the second injection in B16.F10-OVA and thirty-one days following the third injection in MC38-OVA, mice were administered $5x10^5$ B16.F10-OVA or $1x10^6$ MC38-OVA cells suspended in 100 µL PBS on the right flank. Tumor volume was measured every other day *via* caliper measurements and volumes were calculated using:

$$\boldsymbol{V_{tumor} = 0.5 \times L \times W^2}$$

In which V_{tumor} is the tumor volume in mm^3, L is the tumor length in mm, and W is the tumor width in mm. Mice were euthanized via CO_2 asphyxiation when an established endpoint volume of 2000 mm^3 was reached in the study described in **Fig. 3I** or 1500 mm^3 was reached in the study described in **Fig. 3L**.

Pharmacokinetic Cy5 Analysis

6-8 weeks old female C57Bl/6j mice (The Jackson Laboratory) were treated SC at the left base-of-tail with 2 nmol Cy5-labeled nanobody. Blood draws were collected from the tail vein using heparinized capillary tubes (DWK Life Sciences) at indicated timepoints up to 24 h post injection. Following blood collection, blood was diluted 1:50 in PBS, transferred to a 96 well black-walled opaque plate, and analyzed via fluorescence spectroscopy (BioTek Synergy H1) using an excitation wavelength of 645 nm and emission wavelength of 675 nm. A standard curve of nAlb-Cy5 in PBS was used to determine plasma Cy5 concentration. Pharmacokinetic analysis was performed in GraphPad Prism (v10.6.1) using a two-compartmental one-phase absorption and one-phase elimination model of SC injection:

$$\boldsymbol{C = F \times C_0 \times K_a \div (K_a - K_e) \times (e^{-Ke \times t} - e^{-Ka \times t})},$$

where C is the serum concentration of Cy5 over time, C_0 is the initial serum concentration, and F is the fraction of the injection that reaches systemic circulation. C_0 was established assuming a 1.44 mL blood volume for a 20 g mouse[106] and K_e was determined using our previously reported intravenous fits[62]. Curves were fit using nonlinear regression with GraphPad Prism software version 10.6.1.

Flow Cytometry of Tumors

6-8 weeks old female C57Bl/6j mice (The Jackson Laboratory) were treated SC at the left base-of-tail with indicated nanobody-antigen fusion and/or 1.25 µg nAlb-diABZI. Mice were euthanized via CO_2 asphyxiation at indicated timepoints. Tumors were excised, rinsed in PBS, and transferred to a gentleMACS™ C Tube (Miltenyi) for processing using a mouse Tumor Dissociation Kit (Miltenyi) according to the manufacturer's instructions. Cells were rinsed in flow buffer (PBS containing 2% FBS) followed by incubation in tetramer if applicable for 2 h at 4 °C, followed by Fc-block (anti-mouse CD16/CD32, Cytek Biosciences) for 15 min at 4 °C. Cells were then stained with indicated antibodies for 30 min at 4 °C, rinsed with flow buffer, fixed with 2% paraformaldehyde (PFA) in PBS (Thermo Fisher Scientific), rinsed with flow buffer again, and resuspended in 100 uL flow buffer for analysis. For cells analyzed using panels containing intracellular markers, instead of fixing with 2% PFA, cells were fixed using fixation solution from a eBioscience™ Foxp3 / Transcription Factor Fixation/Permeabilization Concentrate and Diluent kit (ThermoFisher) and stained with intracellular antibodies for an additional 30 min at RT prior to rinsing and resuspending in 100 uL flow buffer for analysis. Data was collected using a Cytek Northern Lights multispectral flow cytometer and analyzed using FlowJo (BD Biosciences, version 10.10.0).

Flow Cytometry of Spleens

6-8 weeks old female C57Bl/6j mice (The Jackson Laboratory) were treated SC at the left base-of-tail with indicated nanobody-antigen fusion and/or 1.25 µg nAlb-diABZI. Mice were euthanized via CO_2 asphyxiation at indicated timepoints. Spleens were excised, rinsed in PBS, and transferred to a 70 µm cell strainer (Fisher Scientific) where they were mashed into a single cell suspension. Erythrocytes were removed by incubating splenocytes in 3 mL ACK Lysing Buffer (KD Medical) for 5 min. Splenocytes were rinsed in flow buffer (PBS containing 2% FBS) followed by incubation in tetramer if applicable for 2 h at 4 °C, followed by Fc-block (anti-mouse CD16/CD32, Cytek Biosciences) for 15 min at 4 °C. Splenocytes were then stained with indicated antibodies for 30 min at 4 °C, rinsed with flow buffer, fixed with 2% paraformaldehyde (PFA) in PBS (Thermo Fisher Scientific), rinsed with flow buffer again, and resuspended in 100 uL flow buffer for analysis. For splenocytes analyzed using panels containing intracellular markers, instead of fixing with 2% PFA, splenocytes were fixed using fixation solution from a eBioscience™ Foxp3 / Transcription Factor Fixation/Permeabilization Concentrate and Diluent kit (ThermoFisher) and stained with intracellular antibodies for an additional 30 min at RT prior to rinsing and resuspending in 100 uL flow buffer for analysis. Data was collected using a Cytek Northern Lights multispectral flow cytometer and analyzed using FlowJo (BD Biosciences, version 10.10.0).

Synthesis and Characterization of OVA mRNA LNPs

LNPs were formulated as described previously[107]. In brief, lipids (Avanti Research) were dissolved in ethanol at the following mass fractions of total lipid: ALC-0315 (0.547), DSPC (0.135), cholesterol (0.254), and DMG-PEG2000 (0.064), and warmed to 65 °C. OVA mRNA (Helix Biotech) was diluted in 10 mM citrate buffer (pH 3) and the aqueous and ethanol phases were combined at a 3:1 (v/v) ratio by pipette mixing for 3 min at an N:P ratio of 9.4 (2.5wt% OVA mRNA). The resulting LNPs were buffer exchanged into PBS (pH 7.4) using a 15 mL 10 kDa MWCO Amicon centrifugal filter unit to remove ethanol and residual citrate. OVA mRNA concentration was quantified using a Quant-it™ RiboGreen dye-exclusion assay (ThermoFisher) per the manufacturer's instructions.

Therapeutic Tumor Models

6-8 weeks old female C57Bl/6j mice (The Jackson Laboratory) were inoculated SC with $1x10^6$ YUMM-OVA cells, $5x10^5$ B16.F10-OVA cells, or $3x10^5$ TC-1 cells suspended in 100 µL PBS on the right flank. For the TC-1 re-challenge study in **Fig. 7R**, $3x10^5$ TC-1 cells suspended in 100 µL PBS were inoculated SC on the left flank. Tumor volume was measured every other day *via* caliper measurements and volumes were calculated using:

$$\boldsymbol{V_{tumor} = 0.5 \times L \times W^2}$$

In which V_{tumor} is the tumor volume in mm^3, L is the tumor length in mm, and W is the tumor width in mm.

Treatments began when the average tumor volume reached ~50-150 mm^3, and mice were treated 2-3 times 4 days apart with indicated formulations (5.88 nmol nAlb-$OVA_{251-270}$, 5.88 nmol nAlb-$E7_{38-57}$, 1.25 μg nAlb-diABZI, 5.88 nmol $OVA_{251-270}$ peptide, 50 μg poly(I:C) (pI:C) (Invivogen), and/or 1 μg OVA mRNA encapsulated within LNPs. Mice were euthanized via CO_2 asphyxiation when an established endpoint volume of 1500 mm^3 **(Fig. S44B)** or 2000 mm^3 **(Fig. 6M, Fig. 7B, Fig. 7F, Fig. 7N, and Fig. 7R)** was reached.

Synthesis and Characterization of $OVA_{251-270}$ Peptide

Synthesis of $OVA_{251-270}$ was performed on a Liberty Blue 2.0 microwave peptide synthesizer (CEM Corporation) using Fmoc-protected amino acids and pre-loaded polystyrene resins (CEM Corporation) with the manufacturer's recommended coupling methods. Peptides were cleaved and deprotected by incubation in cleavage cocktail (92.5% trifluoracetic acid (TFA) (Sigma Aldrich), 2.5% triisopropylsilane (TIPS) (Arctom Scientific), 2.5% 3,6-dioxa-1,8-octanedithiol (DODT) (Tokyo Chemical Industry Co.), and 2.5% DI H_2O) for 3 h at RT with stirring. Cleaved peptides were first purified via 3-5 precipitations into cold diethyl ether (Fisher Scientific) and dried under vacuum for 48 h. Peptides were additionally purified using semi-preparative high performance liquid chromatography (HPLC) on a C18 reversed phase HPLC column (Thermo Scientific) using a Waters 1525 Binary HPLC Pump connected to a Waters 2489 UV/Visible Detector and Waters Fraction Collector III (Waters Corporation) with a water:acetonitrile (AN) elution gradient. AN was removed using rotary evaporation (Buchi) and water was subsequently removed via lyophilization (Labconco). Lyophilized peptides were characterized using analytical HPLC on a C18 reversed phase HPLC column (Phenomenex) using a Waters e2695 Separations Module connected to a Waters 2998 PDA Detector (Waters Corporation) **(Fig. S51A)** and liquid chromatography coupled mass spectroscopy (LC-MS) on an Orbitrap XL (Thermo Scientific) **(Fig. S51B)** courtesy of the Vanderbilt University Mass Spectrometry Research Center (MSRC) Core Facility and stored at -20 °C until use.

Statistical Analyses

All statistical analyses were performed using GraphPad Prism software version 10.6.1. All graphs depict mean ± SEM unless otherwise indicated. For most studies, data was analyzed via one-way or two-way ANOVA with Tukey's *post-hoc* or via Welch's two-tailed t test as indicated. Prior to ANOVA analyses, outliers were removed from datasets using the Robust Outlier (ROUT) method with a $Q = 1\%$. For tumor growth curves, the area under the curve (AUC) from Day 0 thru the day of the first death of any mouse in an indicated group was calculated for each individual mouse and analyzed via one-way ANOVA with Tukey's *post-hoc* or via Welch's two-tailed t test as indicated to evaluate differences in growth rates. Survival curves were analyzed via Mantel–Cox log-rank test. ****$P < 0.0001$. ***$P < 0.001$. **$P < 0.01$. *$P < 0.05$.

REFERENCES

1. Haanen, J. B., Schumacher, T. N. M., Kagan, J. C., Fritsch, E. F. & Wu, C. J. Clinical development of cancer vaccines. *Nat. Med.* **32**, 828–840 (2026).

2. Zaidi, N., Jaffee, E. M. & Yarchoan, M. Recent advances in therapeutic cancer vaccines. *Nat. Rev. Cancer* **25**, 517–533 (2025).

3. Weber, J. S. *et al.* Individualised neoantigen therapy mRNA-4157 (V940) plus pembrolizumab versus pembrolizumab monotherapy in resected melanoma (KEYNOTE-942): a randomised, phase 2b study. *The Lancet* **403**, 632–644 (2024).

4. Khattak, A. *et al.* Intismeran Autogene Plus Pembrolizumab Versus Pembrolizumab Alone in High-Risk Resected Melanoma: 5-Year Update of the Randomized Phase IIb KEYNOTE-942 Study. *Journal of Clinical Oncology* **44**, 2482–2489 (2026).

5. *Merck and Moderna Announce Phase 3 INTerpath-001 Trial of Intismeran Autogene Plus KEYTRUDA® Met Endpoints of Recurrence-Free Survival (RFS) and Distant Metastasis-Free Survival (DMFS) in Patients With Completely Resected Stage IIB-IV Melanoma*. (2026).

6. Emens, L. A. *et al.* Challenges and opportunities in cancer immunotherapy: A Society for Immunotherapy of Cancer (SITC) strategic vision. *J. Immunother. Cancer* **12**, (2024).

7. Mellman, I., Chen, D. S., Powles, T. & Turley, S. J. The cancer-immunity cycle: Indication, genotype, and immunotype. *Immunity* **56**, 2188–2205 (2023).

8. Zamora, A. E., Crawford, J. C. & Thomas, P. G. Hitting the Target: How T Cells Detect and Eliminate Tumors. *The Journal of Immunology* **200**, 392–399 (2018).

9. Peng, K., Zhao, X., Fu, Y.-X. & Liang, Y. Eliciting antitumor immunity via therapeutic cancer vaccines. *Cell. Mol. Immunol.* **22**, 840–868 (2025).

10. Khleif, S. N. & Gupta, S. Cancer vaccines as enablers of immunotherapy. *Nat. Immunol.* **26**, 1877–1889 (2025).

11. Saxena, M., van der Burg, S. H., Melief, C. J. M. & Bhardwaj, N. Therapeutic cancer vaccines. *Nat. Rev. Cancer* **21**, 360–378 (2021).

12. Fan, T. *et al.* Therapeutic cancer vaccines: advancements, challenges and prospects. *Signal Transduct. Target. Ther.* **8**, 450 (2023).

13. Wang, Y. *et al.* Challenges and opportunities on achieving an adequate delivery efficiency and immunogenicity with peptide-based anticancer vaccines. *Adv. Drug Deliv. Rev.* **225**, 115675 (2025).

14. Ben-Akiva, E., Chapman, A., Mao, T. & Irvine, D. J. Linking vaccine adjuvant mechanisms of action to function. *Sci. Immunol.* **10**, 5937 (2025).

15. Baretti, M. *et al.* 641 A pilot study of a DNAJB1-PRKACA fusion kinase peptide vaccine combined with nivolumab and ipilimumab for patients with fibrolamellar hepatocellular carcinoma. in *Regular and Young Investigator Award Abstracts* A733–A734 (BMJ Publishing Group Ltd, 2023). doi:10.1136/jitc-2023-SITC2023.0641.

16. Wainberg, Z. A. *et al.* Lymph node-targeted, mKRAS-specific amphiphile vaccine in pancreatic and colorectal cancer: phase 1 AMPLIFY-201 trial final results. *Nat. Med.* **31**, 3648–3653 (2025).

17. Ott, P. A. *et al.* An immunogenic personal neoantigen vaccine for patients with melanoma. *Nature* **547**, 217–221 (2017).

18. Ott, P. A. *et al.* A Phase Ib Trial of Personalized Neoantigen Therapy Plus Anti-PD-1 in Patients with Advanced Melanoma, Non-small Cell Lung Cancer, or Bladder Cancer. *Cell* **183**, 347-362.e24 (2020).

19. Pant, S. *et al.* Lymph-node-targeted, mKRAS-specific amphiphile vaccine in pancreatic and colorectal cancer: the phase 1 AMPLIFY-201 trial. *Nat. Med.* **30**, 531–542 (2024).

20. Braun, D. A. *et al.* A neoantigen vaccine generates antitumour immunity in renal cell carcinoma. *Nature* **639**, 474–482 (2025).

21. Haldar, S. D. *et al.* First-in-Human Testing of a Mutant KRAS Vaccine for Pancreatic Cancer Interception in High-risk Cohorts. *Cancer Discov.* OF1–OF14 (2026) doi:10.1158/2159-8290.CD-25-2245.

22. Verma, N. K. *et al.* Obstacles for T-lymphocytes in the tumour microenvironment: Therapeutic challenges, advances and opportunities beyond immune checkpoint. *EBioMedicine* **83**, 104216 (2022).

23. Hu, M.-M. *et al.* Tumor Microenvironment: Obstacles and Opportunities for T Cell–Based Tumor Immunotherapies. *Molecular Cancer Research* **23**, 277–287 (2025).

24. Peske, J. D., Woods, A. B. & Engelhard, V. H. Control of CD8 T-Cell Infiltration into Tumors by Vasculature and Microenvironment. in *Advances in Cancer Research* vol. 128 263–307 (Academic Press Inc., 2015).

25. Jæhger, D. E. *et al.* Enhancing adoptive CD8 T cell therapy by systemic delivery of tumor associated antigens. *Sci. Rep.* **11**, 19794 (2021).

26. Nagarsheth, N. B. *et al.* TCR-engineered T cells targeting E7 for patients with metastatic HPV-associated epithelial cancers. *Nat. Med.* **27**, 419–425 (2021).

27. Sterner, R. C. & Sterner, R. M. CAR-T cell therapy: current limitations and potential strategies. *Blood Cancer J.* **11**, 69 (2021).

28. Rosenberg, S. A. & Restifo, N. P. Adoptive cell transfer as personalized immunotherapy for human cancer. *Science.* **348**, 62–68 (2015).

29. Soares, K. C. *et al.* PD-1/PD-L1 Blockade Together With Vaccine Therapy Facilitates Effector T-Cell Infiltration Into Pancreatic Tumors. *Journal of Immunotherapy* **38**, 1–11 (2015).

30. Karyampudi, L. *et al.* Accumulation of Memory Precursor CD8 T Cells in Regressing Tumors following Combination Therapy with Vaccine and Anti-PD-1 Antibody. *Cancer Res.* **74**, 2974–2985 (2014).

31. Baljon, J. J. *et al.* A Cancer Nanovaccine for Co-Delivery of Peptide Neoantigens and Optimized Combinations of STING and TLR4 Agonists. *ACS Nano* **18**, 6845–6862 (2024).

32. Lopez, J. *et al.* Autogene cevumeran with or without atezolizumab in advanced solid tumors: a phase 1 trial. *Nat. Med.* **31**, 152–164 (2025).

33. Mendez-Gomez, H. R. *et al.* RNA aggregates harness the danger response for potent cancer immunotherapy. *Cell* **187**, 2521-2535.e21 (2024).

34. Tang, T. *et al.* Advantages of targeting the tumor immune microenvironment over blocking immune checkpoint in cancer immunotherapy. *Signal Transduct. Target. Ther.* **6**, 72 (2021).

35. Xie, Y.-J. *et al.* Overcoming Suppressive Tumor Microenvironment by Vaccines in Solid Tumor. *Vaccines (Basel).* **11**, 394 (2023).

36. Baharom, F., Hermans, D., Delamarre, L. & Seder, R. A. Vax-Innate: improving therapeutic cancer vaccines by modulating T cells and the tumour microenvironment. *Nat. Rev. Immunol.* **25**, 195–211 (2025).

37. Sahin, U. *et al.* Individualized mRNA vaccines evoke durable T cell immunity in adjuvant TNBC. *Nature* **651**, 1088–1096 (2026).

38. Baharom, F. *et al.* Intravenous nanoparticle vaccination generates stem-like TCF1+ neoantigen-specific CD8+ T cells. *Nat. Immunol.* **22**, 41–52 (2021).

39. Baharom, F. *et al.* Systemic vaccination induces CD8+ T cells and remodels the tumor microenvironment. *Cell* **185**, 4317-4332.e15 (2022).

40. Vormehr, M. *et al.* Dexamethasone premedication suppresses vaccine-induced immune responses against cancer. *Oncoimmunology* **9**, (2020).

41. Nel, A. E., Luo, L., Liao, Y.-P. & Wang, X. Reprogramming Immunosuppressive Niches and the Cancer Immunity Cycle in Pancreatic Cancer with Neoantigen mRNA Plus Immune Adjuvant Nanocarrier Strategies. *ACS Nano* **19**, 40733–40745 (2025).

42. Marks, A. *et al.* mRNA vaccine immunity is enhanced by hepatocyte detargeting and not dependent on dendritic cell expression. *Nat. Biotechnol.* https://doi.org/10.1038/s41587-026-03099-z (2026) doi:10.1038/s41587-026-03099-z.

43. Thomson, A. W. & Knolle, P. A. Antigen-presenting cell function in the tolerogenic liver environment. *Nat. Rev. Immunol.* **10**, 753–766 (2010).

44. Rutili, G. & Arfors, K. Protein Concentration in Interstitial and Lymphatic Fluids from the Subcutaneous Tissue. *Acta Physiol. Scand.* **99**, 1–8 (1977).

45. Liang, X. *et al.* Extracellular vesicles engineered to bind albumin demonstrate extended circulation time and lymph node accumulation in mouse models. *J. Extracell. Vesicles* **11**, (2022).

46. Mehta, N. K. *et al.* Pharmacokinetic tuning of protein–antigen fusions enhances the immunogenicity of T-cell vaccines. *Nat. Biomed. Eng.* **4**, 636–648 (2020).

47. Liu, H. *et al.* Structure-based programming of lymph-node targeting in molecular vaccines. *Nature* **507**, 519–522 (2014).

48. Abdallah, M. *et al.* Lymphatic targeting by albumin-hitchhiking: Applications and optimisation. *Journal of Controlled Release* **327**, 117–128 (2020).

49. Supersaxo, A., Hein, W. R. & Steffen, H. Effect of Molecular Weight on the Lymphatic Absorption of Water-Soluble Compounds Following Subcutaneous Administration. *Pharm. Res.* **7**, 167–169 (1990).

50. Zhu, G. *et al.* Albumin/vaccine nanocomplexes that assemble in vivo for combination cancer immunotherapy. *Nat. Commun.* **8**, 1954 (2017).

51. Commisso, C. *et al.* Macropinocytosis of protein is an amino acid supply route in Ras-transformed cells. *Nature* **497**, 633–637 (2013).

52. Hoogenboezem, E. N. & Duvall, C. L. Harnessing albumin as a carrier for cancer therapies. *Adv. Drug Deliv. Rev.* **130**, 73–89 (2018).

53. Stehle, G. *et al.* Plasma protein (albumin) catabolism by the tumor itself—implications for tumor metabolism and the genesis of cachexia. *Crit. Rev. Oncol. Hematol.* **26**, 77–100 (1997).

54. Fanali, G. *et al.* Human serum albumin: From bench to bedside. *Mol. Aspects Med.* **33**, 209–290 (2012).

55. Kratz, F. Albumin as a drug carrier: Design of prodrugs, drug conjugates and nanoparticles. *Journal of Controlled Release* **132**, 171–183 (2008).

56. Kratz, F. & Beyer, U. Serum Proteins as Drug Carriers of Anticancer Agents: A Review. *Drug Deliv.* **5**, 281–299 (1998).

57. Larsen, M. T., Kuhlmann, M., Hvam, M. L. & Howard, K. A. Albumin-based drug delivery: harnessing nature to cure disease. *Mol. Cell. Ther.* **4**, 3 (2016).

58. Sleep, D., Cameron, J. & Evans, L. R. Albumin as a versatile platform for drug half-life extension. *Biochimica et Biophysica Acta (BBA) - General Subjects* **1830**, 5526–5534 (2013).

59. Zorzi, A., Linciano, S. & Angelini, A. Non-covalent albumin-binding ligands for extending the circulating half-life of small biotherapeutics. *Medchemcomm* **10**, 1068–1081 (2019).

60. Martin, J. T. *et al.* Combined PET and whole-tissue imaging of lymphatic-targeting vaccines in non-human primates. *Biomaterials* **275**, 120868 (2021).

61. Alexander, E. & Leong, K. W. Discovery of nanobodies: a comprehensive review of their applications and potential over the past five years. *J. Nanobiotechnology* **22**, 661 (2024).

62. Kimmel, B. R. *et al.* Potentiating cancer immunotherapies with modular albumin-hitchhiking nanobody–STING agonist conjugates. *Nat. Biomed. Eng.* **9**, 1719–1739 (2025).

63. De Felice, S. *et al.* Crystal structure of human serum albumin in complex with megabody reveals unique human and murine cross-reactive binding site. *Protein Science* **33**, (2024).

64. Woo, S.-R. *et al.* STING-Dependent Cytosolic DNA Sensing Mediates Innate Immune Recognition of Immunogenic Tumors. *Immunity* **41**, 830–842 (2014).

65. Li, W. *et al.* cGAS-STING–mediated DNA sensing maintains CD8+ T cell stemness and promotes antitumor T cell therapy. *Sci. Transl. Med.* **12**, 9013 (2020).

66. Corrales, L. *et al.* Direct Activation of STING in the Tumor Microenvironment Leads to Potent and Systemic Tumor Regression and Immunity. *Cell Rep.* **11**, 1018–1030 (2015).

67. Diner, E. J. *et al.* The Innate Immune DNA Sensor cGAS Produces a Noncanonical Cyclic Dinucleotide that Activates Human STING. *Cell Rep.* **3**, 1355–1361 (2013).

68. Garland, K. M., Sheehy, T. L. & Wilson, J. T. Chemical and Biomolecular Strategies for STING Pathway Activation in Cancer Immunotherapy. *Chem. Rev.* **122**, 5977–6039 (2022).

69. Kong, X. *et al.* STING as an emerging therapeutic target for drug discovery: Perspectives from the global patent landscape. *J. Adv. Res.* **44**, 119–133 (2023).

70. Shae, D. *et al.* Co-Delivery of Peptide Neoantigens and Stimulator of Interferon Genes (STING) Agonists Enhances Response to Cancer Vaccines. *ACS Nano* **14**, 9904–9916 (2020).

71. Chen, S. *et al.* Stimuli-responsive STING nanovaccine for systemic therapy of HPV-induced cancers. *Proceedings of the National Academy of Sciences* **122**, (2025).

72. Song, K. *et al.* Peptide vaccine formulations with structurally distinct STING agonist drugamers induce discrete, efficacious antitumor responses. *Proceedings of the National Academy of Sciences* **122**, (2025).

73. Deng, R. *et al.* Subcutaneous bioavailability of therapeutic antibodies as a function of FcRn binding affinity in mice. *MAbs* **4**, 101–109 (2012).

74. Triacca, V., Güç, E., Kilarski, W. W., Pisano, M. & Swartz, M. A. Transcellular Pathways in Lymphatic Endothelial Cells Regulate Changes in Solute Transport by Fluid Stress. *Circ. Res.* **120**, 1440–1452 (2017).

75. Jumper, J. *et al.* Highly accurate protein structure prediction with AlphaFold. *Nature* **596**, 583–589 (2021).

76. Abramson, J. *et al.* Accurate structure prediction of biomolecular interactions with AlphaFold 3. *Nature* **630**, 493–500 (2024).

77. Chen, I., Dorr, B. M. & Liu, D. R. A general strategy for the evolution of bond-forming enzymes using yeast display. *Proceedings of the National Academy of Sciences* **108**, 11399–11404 (2011).

78. Curtsinger, J. M. & Mescher, M. F. Inflammatory cytokines as a third signal for T cell activation. *Curr. Opin. Immunol.* **22**, 333–340 (2010).

79. Calzascia, T. *et al.* TNF-α is critical for antitumor but not antiviral T cell immunity in mice. *Journal of Clinical Investigation* **117**, 3833–3845 (2007).

80. Temizoz, B. & Ishii, K. J. STING agonists as next-generation vaccine adjuvants: mechanisms, opportunities, and challenges. *Curr. Opin. Virol.* **76**, 101543 (2026).

81. Fuertes Marraco, S. A. *et al.* Novel Murine Dendritic Cell Lines: A Powerful Auxiliary Tool for Dendritic Cell Research. *Front. Immunol.* **3**, (2012).

82. Vatner, R. E. & Janssen, E. M. STING, DCs and the link between innate and adaptive tumor immunity. *Mol. Immunol.* **110**, 13–23 (2019).

83. Muntjewerff, E. M., Meesters, L. D. & van den Bogaart, G. Antigen Cross-Presentation by Macrophages. *Front. Immunol.* **11**, (2020).

84. Fleischer, J. *et al.* Differential expression and function of CD80 (B7-1) and CD86 (B7-2) on human peripheral blood monocytes. *Immunology* **89**, 592–598 (1996).

85. McLellan, A. D., Starling, G. C., Williams, L. A., Hock, B. D. & Hart, D. N. J. Activation of human peripheral blood dendritic cells induces the CD86 co-stimulatory molecule. *Eur. J. Immunol.* **25**, 2064–2068 (1995).

86. Roth, G. A. *et al.* Designing spatial and temporal control of vaccine responses. *Nat. Rev. Mater.* **7**, 174–195 (2021).

87. Ya, Z., Hailemichael, Y., Overwijk, W. & Restifo, N. P. Mouse Model for Pre-Clinical Study of Human Cancer Immunotherapy. *Curr. Protoc. Immunol.* **108**, 20.1.1-20.1.43 (2015).

88. Kaech, S. M., Wherry, E. J. & Ahmed, R. Effector and memory T-cell differentiation: implications for vaccine development. *Nat. Rev. Immunol.* **2**, 251–262 (2002).

89. Böttcher, J. P. & Reis e Sousa, C. The Role of Type 1 Conventional Dendritic Cells in Cancer Immunity. *Trends Cancer* **4**, 784–792 (2018).

90. Zhang, J., Yu, S., Peng, Q., Wang, P. & Fang, L. Emerging mechanisms and implications of cGAS-STING signaling in cancer immunotherapy strategies. *Cancer Biol. Med.* **21**, 1–20 (2024).

91. Meeth, K., Wang, J. X., Micevic, G., Damsky, W. & Bosenberg, M. W. The YUMM lines: a series of congenic mouse melanoma cell lines with defined genetic alterations. *Pigment Cell Melanoma Res.* **29**, 590–597 (2016).

92. Lelliott, E. J. *et al.* A novel immunogenic mouse model of melanoma for the preclinical assessment of combination targeted and immune-based therapy. *Sci. Rep.* **9**, 1225 (2019).

93. Kim, K. H. *et al.* The First-week Proliferative Response of Peripheral Blood PD-1+CD8+ T Cells Predicts the Response to Anti-PD-1 Therapy in Solid Tumors. *Clinical Cancer Research* **25**, 2144–2154 (2019).

94. Kim, K. H. *et al.* The First-week Proliferative Response of Peripheral Blood PD-1+CD8+ T Cells Predicts the Response to Anti-PD-1 Therapy in Solid Tumors. *Clinical Cancer Research* **25**, 2144–2154 (2019).

95. Huang, A. C. *et al.* T-cell invigoration to tumour burden ratio associated with anti-PD-1 response. *Nature* **545**, 60–65 (2017).

96. Blass, E. *et al.* A multi-adjuvant personal neoantigen vaccine generates potent immunity in melanoma. *Cell* **188**, 5125-5141.e27 (2025).

97. Tanaka, Y. Ozoralizumab: first Nanobody® therapeutic for rheumatoid arthritis. *Expert Opin. Biol. Ther.* **23**, 579–587 (2023).

98. Irvine, D. J., Aung, A. & Silva, M. Controlling timing and location in vaccines. *Adv. Drug Deliv. Rev.* **158**, 91–115 (2020).

99. *Elicio Therapeutics Reports Results from Phase 2 AMPLIFY-7P Study and Outlines Refined Phase 3 Development Strategy for ELI-002 7P in Adjuvant Pancreatic Cancer*. (2026).

100. Montauti, E., Oh, D. Y. & Fong, L. CD4+ T cells in antitumor immunity. *Trends Cancer* **10**, 969–985 (2024).

101. Wang, X. *et al.* STING agonist-based ER-targeting molecules boost antigen cross-presentation. *Nature* **641**, 202–210 (2025).

102. Sheehy, T. L. *et al.* STING-Activating Polymer–Drug Conjugates for Cancer Immunotherapy. *ACS Cent. Sci.* **10**, 1765–1781 (2024).

103. Nguyen, D. C. *et al.* Mannosylated STING Agonist Drugamers for Dendritic Cell-Mediated Cancer Immunotherapy. *ACS Cent. Sci.* **10**, 666–675 (2024).

104. Marty, M. T. *et al.* Bayesian Deconvolution of Mass and Ion Mobility Spectra: From Binary Interactions to Polydisperse Ensembles. *Anal. Chem.* **87**, 4370–4376 (2015).

105. Fra-Bido, S., Walker, S. A., Innocentin, S. & Linterman, M. A. Optimized immunofluorescence staining protocol for imaging germinal centers in secondary lymphoid tissues of vaccinated mice. *STAR Protoc.* **2**, 100499 (2021).

106. *Tail Vein Blood Collection in Mice*. https://www.queensu.ca/animals-in-science/policies-procedures/sop/mice/7-10-3 (2012).

107. Wang-Bishop, L. *et al.* Nanoparticle Retinoic Acid-Inducible Gene I Agonist for Cancer Immunotherapy. *ACS Nano* **18**, 11631–11643 (2024).

ACKNOWLEDGEMENTS

We thank C. Duvall for use of the IVIS imaging system, S. Joyce for providing the biotinylated H-2Kb/SIINFEKL monomer that was used to make the PE-labeled H-2Kb/SIINFEKL tetramer, A. Lund for providing the OVA expressing B16.F10 and YUMM cell lines, and D. Mogilenko for providing the MutuDC1940 cell line. We thank the core facilities of the Vanderbilt Ingram Cancer Center (VICC) (P30 CA68485), the Vanderbilt University Small Molecule NMR Facility, the Vanderbilt Center for Structural Biology, the Vanderbilt Mass Spectroscopy Research Center, the Vanderbilt Center for Innovative Technology, and the Vanderbilt Cell Imaging Shared Resource (CISR) supported by NIH grants CA68485, DK20593, DK58404, DK59637, EY08126 and S10 OD021630. J.E.F. and A.L. acknowledge support from the Vanderbilt Undergraduate Summer Research Program (VUSRP).

Funding:

National Institutes of Health R01 CA245134 (J.T.W.)
National Institutes of Health R01 CA266767 (J.T.W.)
VICC Support Grant P30 CA68485 (J.T.W.)
Vanderbilt Ingram Cancer Center (VICC) (J.T.W.)
Vanderbilt University School of Engineering (J.T.W.)

National Institutes of Health T32 CA009592 (A.J.K.)
National Institutes of Health F32 CA288044 (A.J.K.)
National Institutes of Health T32 CA009592 (A.K.V.)
PhRMA Foundation Postdoctoral Fellowship in Drug Delivery (A.K.V., B.R.K.)
NIH Medical Scientist Training Program T32 GM007347 (N.C.C.)
NIH Chemical-Biology Interface Training Grant T32 GM065086 (K.A.Y.)
Cancer Research Institute Postdoctoral Fellowship (E.A.S.)
NIH Integrated Training in Engineering and Diabetes T32 DK101003 (H.M.P.)
National Science Foundation Graduate Research Fellowship (H.M.P, M.E.W., J.A.S.)
National Institutes of Health F30 DK145130 (L.M.C.)
National Institutes of Health T32 GM007347 (L.M.C.)
Breakthrough T1D 2-SRA-2026-1859-S-B (R.H.B.)

Author Contributions:

Conceptualization: H.M.P., B.R.K., J.T.W.
Methodology: H.M.P., N.C.C., A.J.K., A.K.V., B.R.K., K.A., J.T.W.
Formal Analysis: H.M.P.
Investigation: H.M.P., N.C.C., T.M.P., A.J.K., M.E.W., J.A.S., K.A.Y., C.L., E.A.S., J.E.F., A.L., H.J.F., J.C.M., L.M.C., B.R.K., K.A.
Resources: R.H.B., J.A.M., J.T.W.
Data Curation: H.M.P.
Writing – Original Draft: H.M.P., J.T.W.
Writing – Review & Editing: H.M.P., N.C.C., J.T.W.
Visualization: H.M.P., J.T.W.
Supervision: H.M.P., B.R.K., J.T.W.
Project Administration: H.M.P., J.T.W.
Funding Acquisition: H.M.P., N.C.C., A.J.K., M.E.W., J.A.S., K.A.Y., A.K.V., E.A.S., L.M.C., R.H.B., B.R.K., J.T.W.

Competing Interests:

J.T.W., H.M.P., B.R.K., and K.A. have patent PCT/US2024/051131 pending to Vanderbilt University.

J.T.W. has received consulting fees from ADC Therapeutics and has received sponsored research support from Incyte Corporation.

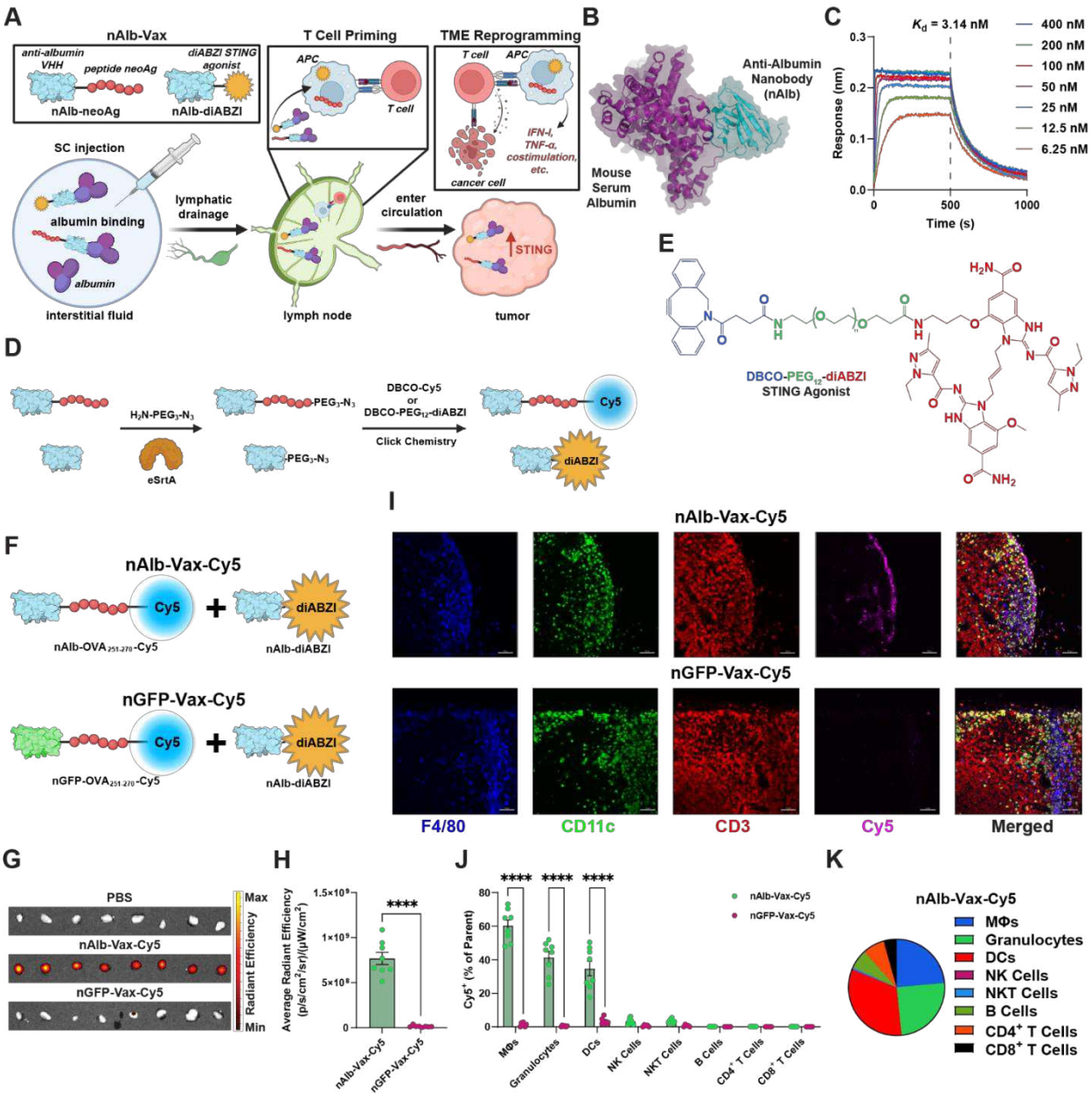


Figure 1. Albumin-binding nanobodies (nAlb) enhance the delivery of peptide antigens and STING agonist adjuvants to antigen-presenting cells (APCs) in the injection-draining lymph node (LN). (A) Schematic depicting proposed mechanism of nAlb-Vax biodistribution and efficacy following SC injection. Created with Biorender.com. **(B)** AlphaFold3 model of nAlb binding MSA. Visualized with PyMOL. **(C)** BLI measurements of nAlb binding to MSA, indicating that binding occurs with nanomolar affinity. **(D)** Schematic depicting the series of sortase and strain-promoted azide-alkyne cycloaddition (SPAAC) reactions used to label nanobodies and nanobody-antigen fusions with diABZI and Cy5, respectively. Created with Biorender.com. **(E)** Chemical structure of DBCO-PEG$_{12}$-diABZI STING agonist containing a dibenzocyclooctyne (DBCO) moiety for SPAAC ligation to azide-functionalized nanobodies. **(F)** Schematic of nAlb-Vax-Cy5 and nGFP-Vax-Cy5 formulations. Created with Biorender.com. **(G)** Representative IVIS images and **(H)** quantification of the average radiant efficiency of Cy5 in the

injection-draining LN 24 h after treatment with indicated constructs (mean ± SEM, n = 8). Analyzed via Welch's two-tailed t test. **(I)** Representative immunofluorescent microscopy (20X magnification) images of the injection-draining LN 24 h after treatment with nAlb-Vax-Cy5 or nGFP-Vax-Cy5 (scale bars, 50 μm). **(J)** Flow cytometric quantification of Cy5 uptake by major immune cell populations within the draining LN (mean ± SEM, n = 8). Analyzed via two-way ANOVA with Tukey's *post-hoc*. **(K)** Pie chart depicting Cy5 uptake by major immune cell populations in the injection-draining LN as a percentage of all $Cy5^+$ cells following treatment with nAlb-Vax-Cy5. ****$P < 0.0001$. ***$P < 0.001$. **$P < 0.01$. *$P < 0.05$.

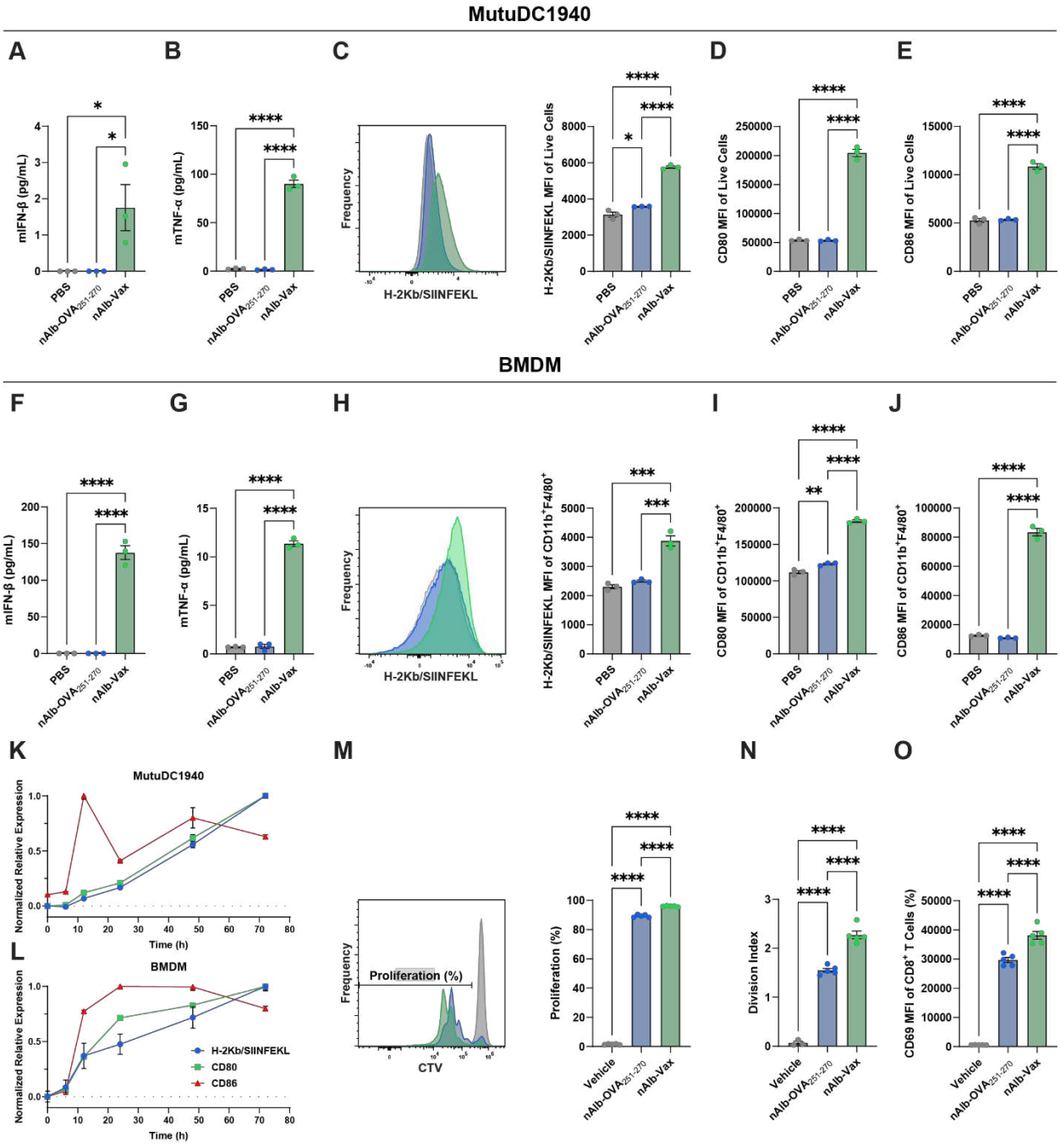


Figure 2. nAlb-Vax induces antigen presentation along with co-stimulation and inflammatory cytokine secretion by antigen-presenting cells (APCs) to induce antigen-specific T cell proliferation. (A) mIFN-β and **(B)** mTNF-α secretion by MutuDC1940 cells 24 h after treatment with indicated constructs (mean ± SEM, *n* = 3). **(C)** Representative histograms and H-2Kb/SIINFEKL MFI indicating H-2Kb/SIINFEKL expression by MutuDC1940 cells 24 h after treatment with indicated formulations (mean ± SEM, *n* = 3). **(D)** CD80 and **(E)** CD86 MFI on MutuDC1940 cells 24 h after treatment with indicated constructs (mean ± SEM, *n* = 3). **(F)** mIFN-β and **(G)** mTNF-α secretion by BMDMs 24 h after treatment with indicated constructs (mean ± SEM, *n* = 3). **(H)** Representative histograms and H-2Kb/SIINFEKL MFI indicating H-

2Kb/SIINFEKL expression by BMDMs 24 h after treatment with indicated constructs (mean ± SEM, n = 3). **(I)** CD80 and **(J)** CD86 MFI on BMDMs 24 h after treatment with indicated constructs (mean ± SEM, n = 3). Normalized relative expression of H-2Kb/SIINFEKL, CD80, and CD86 by **(K)** MutuDC1940 cells and **(L)** BMDMs following treatment with nAlb-Vax for indicated timepoints (mean ± SEM, n = 3). **(M)** Representative histograms and quantification of OT-I T cell proliferation as measured by CTV dilution following treatment with indicated constructs (mean ± SEM, n = 5). **(N)** Division Index, reflecting the average number of cell divisions, of OT-I T cells that have proliferated following treatment with indicated constructs (mean ± SEM, n = 3-5). **(O)** CD69 MFI of OT-I T cells following treatment with indicated constructs (mean ± SEM, n = 5). Analyzed via one-way ANOVA with Tukey's *post-hoc*. ****P < 0.0001. ***P < 0.001. **P < 0.01. *P < 0.05.

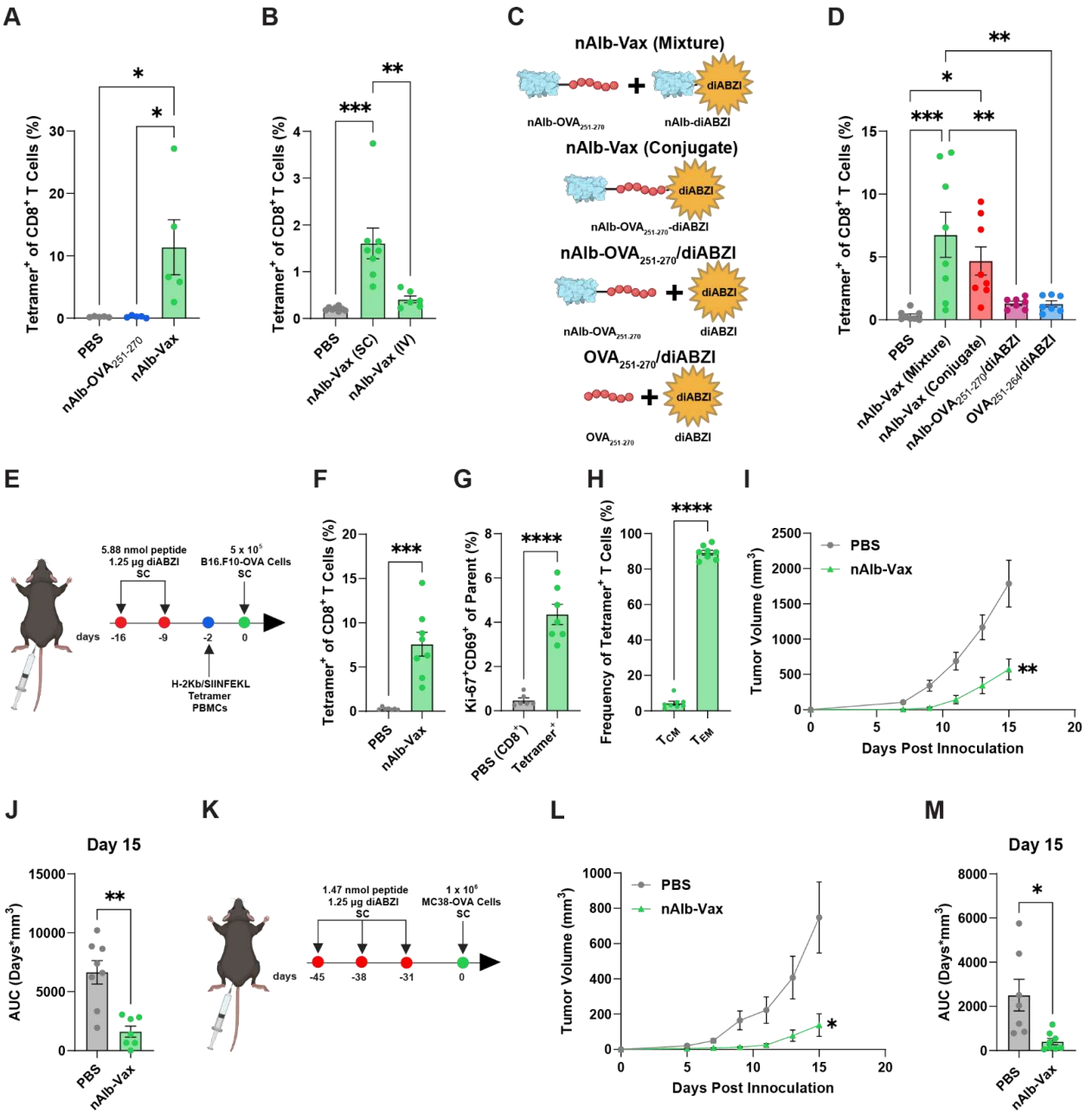


Figure 3. Prophylactic vaccination with nAlb-Vax generates antigen-specific T cells with effector memory phenotype capable of protecting against tumor challenge. (A) Quantification of H-2Kb/SIINFEKL tetramer$^+$ T cells following treatments with indicated formulations (mean ± SEM, n = 5). **(B)** Quantification of H-2Kb/SIINFEKL tetramer$^+$ T cells following treatments with indicated formulations or injection routes (mean ± SEM, n = 6-8). **(C)** Schematic of nAlb-Vax as either a mixture of nAlb-OVA$_{251-270}$ and nAlb-diABZI or a nAlb-OVA$_{251-270}$-diABZI conjugate as well as relevant control formulations. Created with Biorender.com. **(D)** Quantification of H-2Kb/SIINFEKL tetramer$^+$ T cells following treatments with indicated formulations (mean ± SEM, n = 7-8). **(E)** Schematic of treatment timeline. Created with Biorender.com. **(F)** Quantification of H-2Kb/SIINFEKL tetramer$^+$ T cells following treatments with indicated formulations (mean ± SEM, n = 8). **(G)** Frequency of activated, proliferating (CD69$^+$Ki-67$^+$) tetramer$^+$ T cells following

treatment with indicated formulations (mean ± SEM, n = 7-8). **(H)** Frequency of T_{CM} ($CD44^+CD62L^+$) and T_{EM} ($CD44^+CD62L^-$) cells within the tetramer$^+$ T cell population following treatment with nAlb-Vax (mean ± SEM, n = 7-8). **(I)** Tumor growth curves and **(J)** area under the curve (AUC) of individual tumor growth curves following prophylactic vaccination with nAlb-Vax and subsequent challenge with B16.F10-OVA tumors (mean ± SEM, n = 7-8). Analyzed via Welch's two-tailed t test. **(K)** Schematic of treatment timeline. Created with Biorender.com. **(L)** Tumor growth curves and **(M)** AUC of individual tumor growth curves following prophylactic vaccination with nAlb-Vax and subsequent challenge with MC38-OVA tumors (mean ± SEM, n = 7-8). Analyzed via Welch's two-tailed t test. ****$P < 0.0001$. ***$P < 0.001$. **$P < 0.01$. *$P < 0.05$.

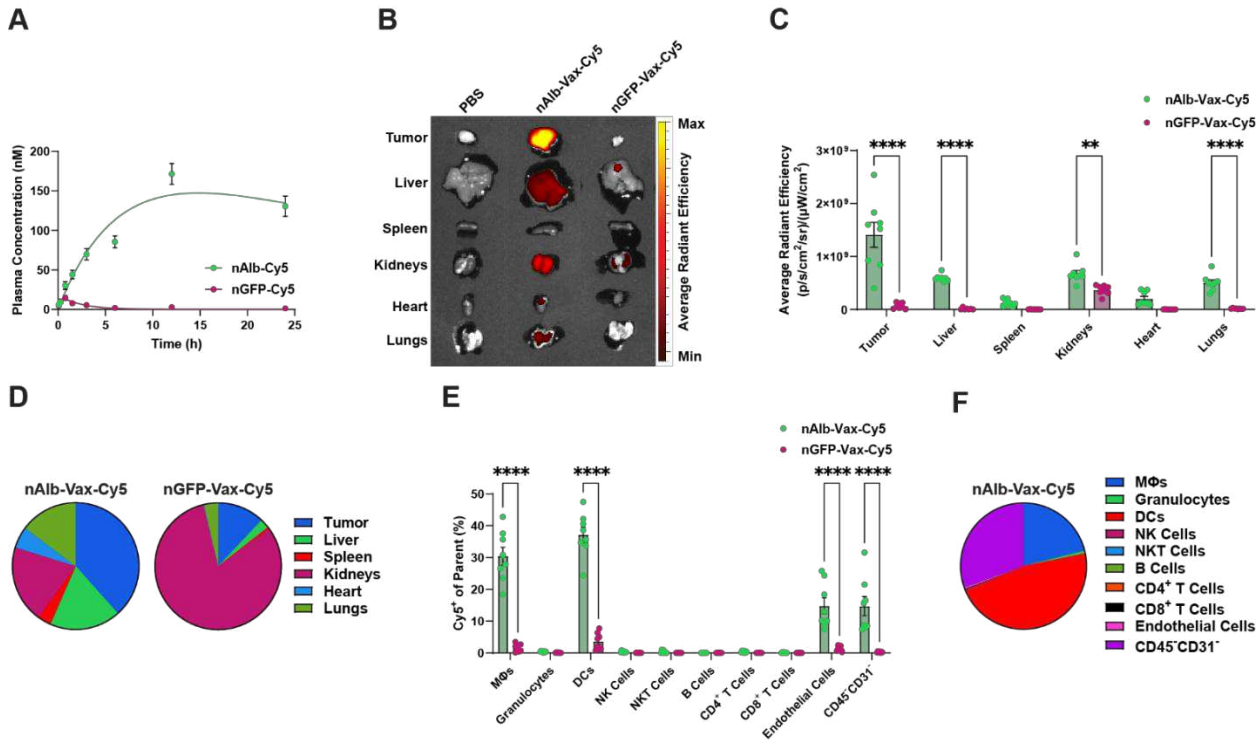


Figure 4. Subcutaneously (SC) administered nAlb-Vax enters systemic circulation after initial lymphatic drainage to accumulate within APCs in the TME. (A) Blood plasma Cy5 concentration at indicated timepoints following SC administration of nAlb-Cy5 or nGFP-Cy5 in healthy C57Bl/6j mice (mean ± SEM, n = 7-8). Fit to a pharmacokinetic model of drug clearance following SC injection. **(B)** Representative IVIS images of tumors and major clearance organs of mice 24 h following SC treatment with indicated constructs. **(C)** Autofluorescence-subtracted average radiant efficiency values of tumors and major clearance organs of mice 24 h following SC treatment with indicated constructs (mean ± SEM, n = 5-7). Analyzed via two-way ANOVA with Tukey's *post-hoc*. **(D)** Pie charts depicting autofluorescence extracted Cy5 accumulation by tumors and major clearance organs in C57Bl/6j mice as a percentage of all detectable Cy5 signal following treatment with indicated constructs. **(E)** Quantification of Cy5 uptake by major cell populations in MC38 tumors 24 h following SC administration of indicated constructs (mean ± SEM, n = 5-7). Analyzed via two-way ANOVA with Tukey's *post-hoc*. **(F)** Pie chart depicting Cy5 uptake by major cell populations in the TME as a percentage of all $Cy5^+$ cells following treatment with nAlb-Vax-Cy5. ****$P < 0.0001$. ***$P < 0.001$. **$P < 0.01$. *$P < 0.05$.

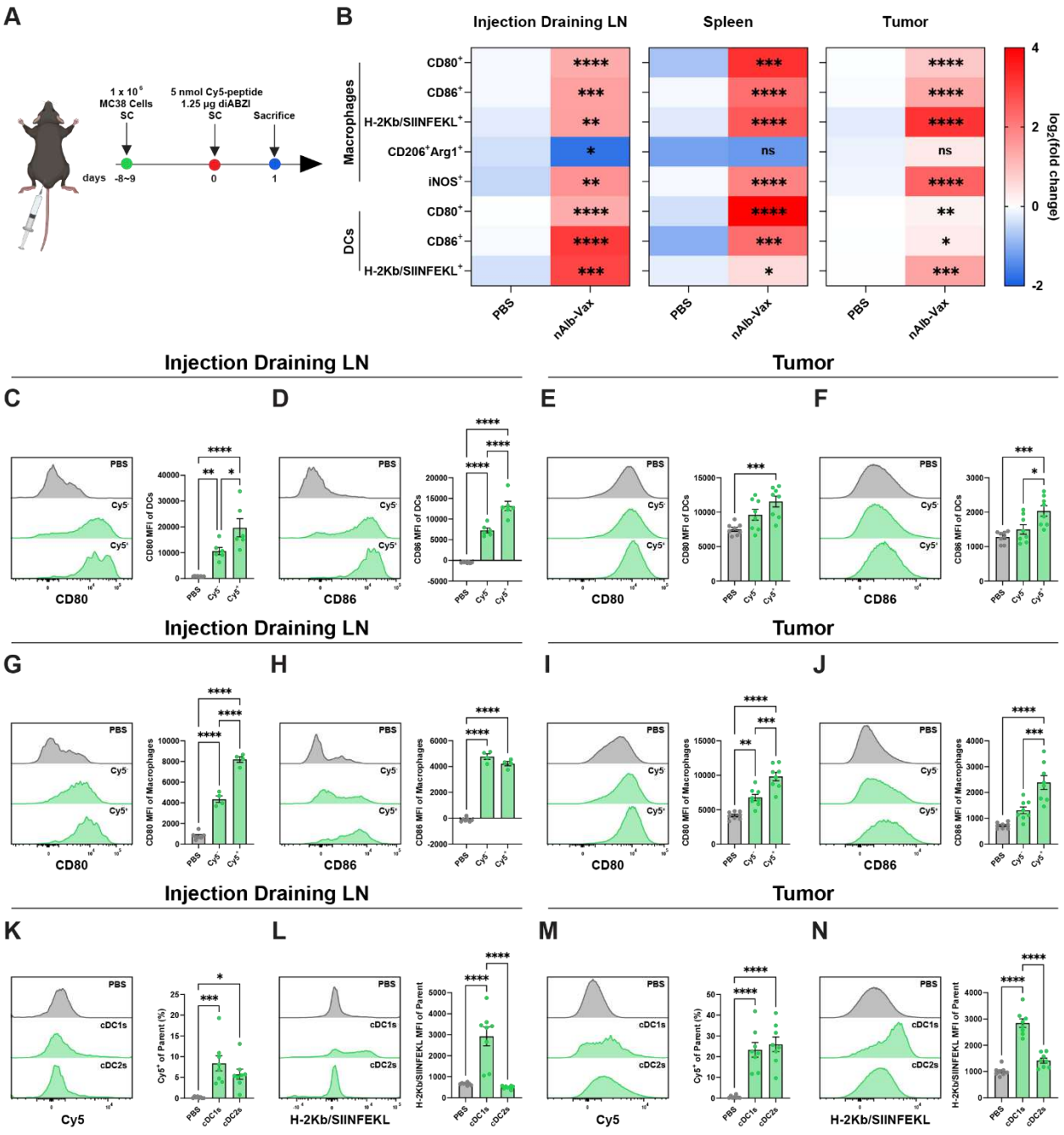


Figure 5. nAlb-Vax activates and induces antigen presentation by APCs, especially cDC1s, in lymphoid tissues and the TME. (A) Timeline of nAlb-Vax-Cy5 myeloid phenotyping study. Created with Biorender.com. **(B)** Heat maps summarizing the $\log_2$(fold change) in the percentage of indicated cell populations relative to PBS control in indicated tissues (n = 6-8). Analyzed via Welch's two-tailed t test. **(C)** Representative histograms and CD80 MFI of indicated DC ($CD11c^+$) populations or treatments in the injection-draining LN 24 h after treatment with PBS or nAlb-Vax-Cy5 (mean ± SEM, n = 6). Analyzed via one-way ANOVA with Tukey's *post-hoc*. **(D)** Representative histograms and CD86 MFI of indicated DC ($CD11c^+$) populations or treatments in the injection-draining LN 24 h after treatment with PBS or nAlb-Vax-Cy5 (mean ± SEM, n = 6). Analyzed via one-way ANOVA with Tukey's *post-hoc*. **(E)** Representative histograms and CD80

MFI of indicated DC ($CD11c^+$) populations or treatments in the TME 24 h after treatment with PBS or nAlb-Vax-Cy5 (mean ± SEM, n = 8). Analyzed via one-way ANOVA with Tukey's *post-hoc*. **(F)** Representative histograms and CD86 MFI of indicated DC ($CD11c^+$) populations or treatments in the TME 24 h after treatment with PBS or nAlb-Vax-Cy5 (mean ± SEM, n = 8). Analyzed via one-way ANOVA with Tukey's *post-hoc*. **(G)** Representative histograms and CD80 MFI of indicated macrophage ($CD11b^+F4/80^+$) populations or treatments in the injection-draining LN 24 h after treatment with PBS or nAlb-Vax-Cy5 (mean ± SEM, n = 4-6). Analyzed via one-way ANOVA with Tukey's *post-hoc*. **(H)** Representative histograms and CD86 MFI of indicated macrophage ($CD11b^+F4/80^+$) populations or treatments in the injection-draining LN 24 h after treatment with PBS or nAlb-Vax-Cy5 (mean ± SEM, n = 4-6). Analyzed via one-way ANOVA with Tukey's *post-hoc*. **(I)** Representative histograms and CD80 MFI of indicated macrophage ($CD11b^+F4/80^+$) populations or treatments in the TME 24 h after treatment with PBS or nAlb-Vax-Cy5 (mean ± SEM, n = 7-8). Analyzed via one-way ANOVA with Tukey's *post-hoc*. **(J)** Representative histograms and CD86 MFI of indicated macrophage ($CD11b^+F4/80^+$) populations or treatments in the TME 24 h after treatment with PBS or nAlb-Vax-Cy5 (mean ± SEM, n = 7-8). Analyzed via one-way ANOVA with Tukey's *post-hoc*. **(K)** Representative histograms and quantification of Cy5 uptake by indicated DC ($CD11c^+$) subpopulation in the injection-draining LN 24 h after treatment with PBS or nAlb-Vax-Cy5 (mean ± SEM, n = 7-8). Analyzed via one-way ANOVA with Tukey's *post-hoc*. **(L)** Representative histograms and quantification of H-2Kb/SIINFEKL MFI by indicated DC ($CD11c^+$) subpopulation in the injection-draining LN 24 h after treatment with PBS or nAlb-Vax-Cy5 (mean ± SEM, n = 7-8). Analyzed via one-way ANOVA with Tukey's *post-hoc*. **(M)** Representative histograms and quantification of Cy5 uptake by indicated DC ($CD11c^+$) subpopulation in the TME 24 h after treatment with PBS or nAlb-Vax-Cy5 (mean ± SEM, n = 8). Analyzed via one-way ANOVA with Tukey's *post-hoc*. **(N)** Representative histograms and quantification of H-2Kb/SIINFEKL MFI by indicated DC ($CD11c^+$) subpopulation in the TME 24 h after treatment with PBS or nAlb-Vax-Cy5 (mean ± SEM, n = 8). Analyzed via one-way ANOVA with Tukey's *post-hoc*. $^{****}P < 0.0001$. $^{***}P < 0.001$. $^{**}P < 0.01$. $^{*}P < 0.05$.

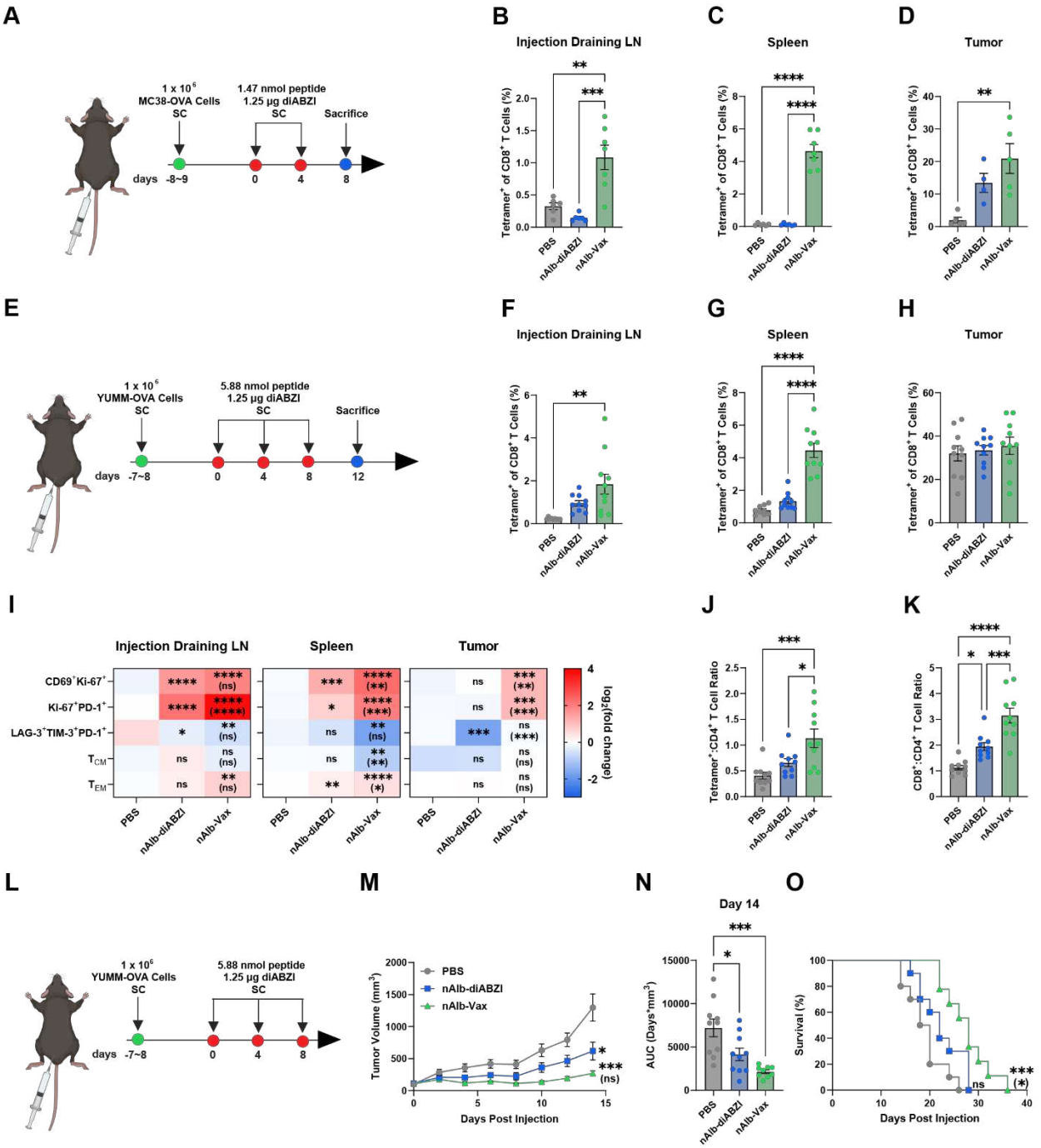


Figure 6. Therapeutic vaccination with nAlb-Vax generates antigen-specific CD8$^+$ T cells in multiple lymphoid tissues and the TME that exhibit an activated, effector memory phenotype. (A) Timeline for tetramer analysis study of lymphoid tissues and the TME in MC38-OVA tumors. Created with Biorender.com. Quantification of the frequency of tetramer$^+$ T cells following vaccination with indicated formulation in the **(B)** injection-draining LN, **(C)** spleen, and **(D)** tumor (mean ± SEM, n = 4-8). **(E)** Timeline for tetramer analysis study of lymphoid tissues and the TME in YUMM-OVA tumors. Created with Biorender.com. Quantification of the frequency of tetramer$^+$ T cells following vaccination with indicated formulation in the **(F)**

injection-draining LN, **(G)** spleen, and **(H)** tumor (mean ± SEM, n = 9-10). **(I)** Heat maps summarizing the $\log_2$(fold change) in the percentage of indicated cell populations relative to PBS control in indicated tissues (n = 6-10). Analyzed via one-way ANOVA with Tukey's *post-hoc*. Stars (*) without parentheses indicate statistical analysis compared to PBS control. Stars (*) inside parentheses indicate statistical analysis compared to nAlb-diABZI control. **(J)** Tetramer$^+$ T cell and **(K)** CD8$^+$ T cell to CD4$^+$ T cell ratio in the TME following treatment with indicated formulations (mean ± SEM, n = 10). **(L)** Timeline of YUMM-OVA inoculation and treatment with indicated constructs. Created with Biorender.com. **(M)** Tumor growth curves, **(N)** AUC of individual tumor growth curves, and **(O)** Kaplan-Meier survival plots following treatment with indicated constructs (mean ± SEM, n = 9-10). Stars (*) without parentheses indicate statistical analysis compared to PBS control. Stars (*) inside parentheses indicate statistical analysis compared to nAlb-diABZI control. Analyzed via one-way ANOVA with Tukey's *post-hoc* or Mantel-Cox log-rank test as appropriate. ****$P < 0.0001$. ***$P < 0.001$. **$P < 0.01$. *$P < 0.05$.

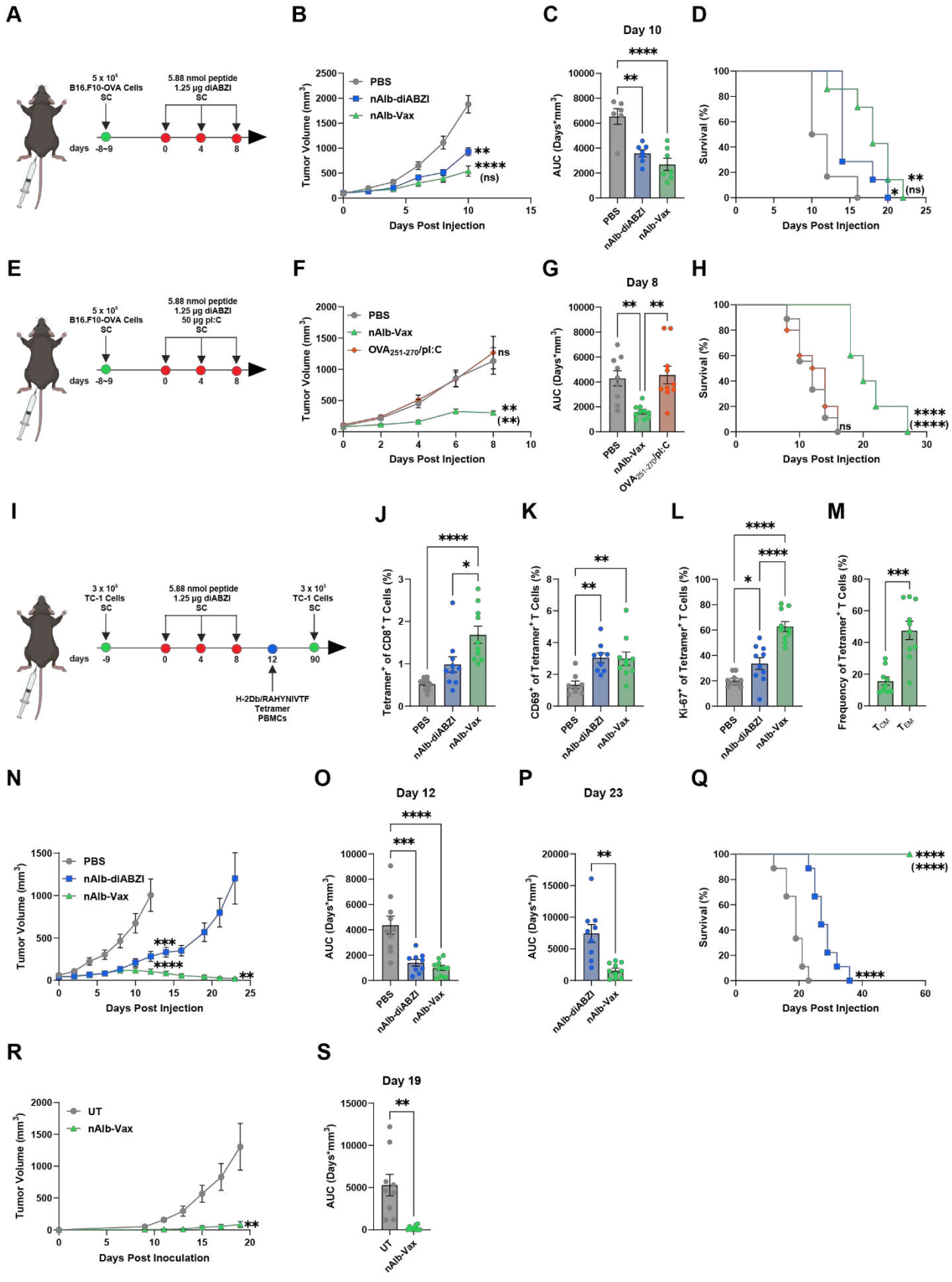

A
5 x 10^5 B16.F10-OVA Cells SC
5.88 nmol peptide 1.25 µg diABZI SC
days -8~9 0 4 8
B
PBS
nAlb-diABZI
nAlb-Vax
Tumor Volume (mm^3)
Days Post Injection
**
****
(ns)
C
Day 10
AUC (Days*mm^3)
PBS
nAlb-diABZI
nAlb-Vax
D
Survival (%)
Days Post Injection
**
*
(ns)
E
5 x 10^5 B16.F10-OVA Cells SC
5.88 nmol peptide 1.25 µg diABZI 50 µg pI:C SC
F
PBS
nAlb-Vax
OVA251-270/pI:C
ns
**
(**)
G
Day 8
H
****
(****)
I
3 x 10^6 TC-1 Cells SC
5.88 nmol peptide 1.25 µg diABZI SC
3 x 10^5 TC-1 Cells SC
days -9 0 4 8 12 90
H-2Db/RAHYNIVTF Tetramer PBMCs
J
Tetramer+ of CD8+ T Cells (%)
K
CD69+ of Tetramer+ T Cells (%)
L
Ki-67+ of Tetramer+ T Cells (%)
M
Frequency of Tetramer+ T Cells (%)
TCM
TEM
N
O
Day 12
P
Day 23
Q
R
UT
nAlb-Vax
Days Post Inoculation
S
Day 19

Figure 7. Therapeutic vaccination with nAlb-Vax generates antitumor immunity and extends survival in multiple murine cancer models and outperforms clinical vaccine candidates. (A) Timeline of B16.F10-OVA inoculation and treatment with indicated constructs. Created with Biorender.com. **(B)** B16.F10-OVA tumor volumes, **(C)** AUC of the individual tumor growth curves, and **(D)** Kaplan-Meier survival plots following treatment with indicated constructs (mean ± SEM, n = 6-7). Stars (*) without parentheses indicate statistical analysis compared to PBS control. Stars (*) inside parentheses indicate statistical analysis compared to nAlb-diABZI control. Analyzed via one-way ANOVA with Tukey's *post-hoc* or Mantel-Cox log-rank test as appropriate. **(E)** Timeline of B16.F10-OVA inoculation and treatment with indicated constructs. Created with Biorender.com. **(F)** B16.F10-OVA tumor volumes, **(G)** AUC of the individual tumor growth curves, and **(H)** Kaplan-Meier survival plots following treatment with indicated constructs (mean ± SEM, n = 9-10). Stars (*) without parentheses indicate statistical analysis compared to PBS control. Stars (*) inside parentheses indicate statistical analysis compared to $OVA_{251-270}$/pI:C control. Analyzed via one-way ANOVA with Tukey's *post-hoc* or Mantel-Cox log-rank test as appropriate. **(I)** Timeline of TC-1 inoculation, treatment with indicated constructs, and PBMC tetramer analysis. Created with Biorender.com. **(J)** Frequency of H-2Db/RAHYNIVTF tetramer$^+$ T cells following vaccination with indicated constructs (mean ± SEM, n = 10). Frequency of **(K)** activated (CD69$^+$) and **(L)** proliferating (Ki-67$^+$) tetramer$^+$ T cells following vaccination with indicated constructs (mean ± SEM, n = 10). Analyzed via one-way ANOVA with Tukey's *post-hoc*. **(M)** Frequency of T_{CM} (CD44$^+$CD62L$^+$) and T_{EM} (CD44$^+$CD62L$^-$) cells within the tetramer$^+$ T cell population following treatment with nAlb-Vax (mean ± SEM, n = 10). Analyzed via Welch's two-tailed t test. **(N)** TC-1 tumor volumes, **(O)** AUC of individual tumor growth curves from Day 0 thru Day 12 when the first mouse in the PBS group died, and **(P)** AUC of individual tumor growth curves from Day 0 thru Day 23 when the first mouse in the nAlb-diABZI group died (mean ± SEM, n = 9-10). Analyzed via one-way ANOVA with Tukey's *post-hoc* or Welch's two-tailed t test as appropriate. **(Q)** Kaplan-Meier survival plots following treatment with indicated constructs (mean ± SEM, n = 9-10). Analyzed via Mantel-Cox log-rank test. Stars (*) without parentheses indicate statistical analysis compared to PBS control. Stars (*) inside parentheses indicate statistical analysis compared to nAlb-diABZI control. **(R)** TC-1 tumor volumes and **(S)** AUC of the individual tumor growth curves (mean ± SEM, n = 9). Analyzed via Welch's two-tailed t test. ****$P < 0.0001$. ***$P < 0.001$. **$P < 0.01$. *$P < 0.05$.

Supplementary Files

This is a list of supplementary files associated with this preprint. Click to download.

- PagendarmetalNatureBMESupplementaryInformation.pdf